2021

Fast inactivation of Nav current in rat adrenal chromaffin cells involves two independent inactivation pathways

Pedro L. Martinez-Espinosa

Alan Neely

Jiuping Ding

Christopher J. Lingle

JGP Journal of General Physiology

ARTICLE

Fast inactivation of Nav current in rat adrenal chromaffin cells involves two independent inactivation pathways

Pedro L. Martinez-Espinosa, Alan Neely, Jiuping Ding, and Christopher J. Lingle

Voltage-dependent sodium (Nav) current in adrenal chromaffin cells (CCs) is rapidly inactivating and tetrodotoxin (TTX)–sensitive. The fractional availability of CC Nav current has been implicated in regulation of action potential (AP) frequency and the occurrence of slow-wave burst firing. Here, through recordings of Nav current in rat CCs, primarily in adrenal medullary slices, we describe unique inactivation properties of CC Nav inactivation that help define AP firing rates in CCs. The key feature of CC Nav current is that recovery from inactivation, even following brief (5 ms) inactivation steps, exhibits two exponential components of similar amplitude. Various paired pulse protocols show that entry into the fast and slower recovery processes result from largely independent competing inactivation pathways, each of which occurs with similar onset times at depolarizing potentials. Over voltages from −120 to −80 mV, faster recovery varies from ∼3 to 30 ms, while slower recovery varies from ∼50 to 400 ms. With strong depolarization (above −10 mV), the relative entry into slow or fast recovery pathways is similar and independent of voltage. Trains of short depolarizations favor recovery from fast recovery pathways and result in cumulative increases in the slow recovery fraction. Dual-pathway fast inactivation, by promoting use-dependent accumulation in slow recovery pathways, dynamically regulates Nav availability. Consistent with this finding, repetitive AP clamp waveforms at 1–10 Hz frequencies reduce Nav availability 80–90%, depending on holding potential. These results indicate that there are two distinct pathways of fast inactivation, one leading to conventional fast recovery and the other to slower recovery, which together are well-suited to mediate use-dependent changes in Nav availability.

Introduction

A classic view of the role of voltage-dependent Na^+ (Nav) current is that it supports the reliable generation of action potentials (APs) of uniform duration and amplitude (Hille, 2001). This requires a sequence of rapid Nav current activation to produce cell depolarization, subsequent inactivation to help terminate net inward current, and then recovery from inactivation to permit a subsequent AP. The time course of recovery from rapid inactivation of Nav current contributes to a refractory period during which a cell is unable to generate a full AP (Hodgkin and Huxley, 1952; Kuo and Bean, 1994; Hille, 2001), potentially limiting cell firing rates. However, in many cells, recovery from fast inactivation is sufficiently rapid that repetitive AP firing can be sustained with little diminution in AP amplitude or change in AP frequency at AP frequencies >50 Hz (Schwindt et al., 1988; Wang et al., 1998; Khaliq et al., 2003; Kaczmarek et al., 2005; Brickley et al., 2007; Carter and Bean, 2011). However, in addition to fast inactivation, many Nav currents also exhibit an inactivation behavior in which recovery from inactivation occurs much more slowly, over hundreds of milliseconds or even seconds (Chiu, 1977; Rudy, 1981; Belluzzi and Sacchi, 1986; Jones, 1987; Ruff, 1996; Zhang et al., 2013; Silva, 2014). Such inactivation is sufficiently slow in onset that only in some unusual circumstances is it likely to influence Nav availability during normal firing (Silva, 2014).

Over the past 15 yr, the identification of additional Nav variants with distinct kinetic properties has helped unveil the remarkable complexity of Nav current behavior in native cells (Cummins et al., 1998; Dib-Hajj et al., 1999; Cummins et al., 2001; Hains et al., 2003; Herzog et al., 2003; Liu et al., 2003; Rush et al., 2006; Choi et al., 2007; Goldfarb et al., 2007; Milescu et al., 2010) and has increased awareness that patterns of AP firing may be influenced by use-dependent changes in availability of

Department of Anesthesiology, Washington University School of Medicine, St. Louis, MO.

Correspondence to Christopher J. Lingle: clingle@wustl.edu; A. Neely's present address is Facultad de Ciencias, Centro Interdisciplinario de Neurociencia de Valparaiso, Instituto de Neurociencia, Universidad de Valparaiso, Valparaiso, Chile; J. Ding has retired and is no longer affiliated with any institution. A preprint of this paper was posted in *bioRxiv* on November 1, 2020.

Nav channels. Furthermore, new mechanisms by which Nav channels can be regulated have been identified (Goldfarb, 2005; Rush et al., 2006; Goldfarb et al., 2007; Laezza et al., 2009; Shakkottai et al., 2009; Bosch et al., 2015). Specifically, for some Nav currents, recovery from inactivation can occur at rates intermediate between traditional fast and slow recovery, involving a mechanism that appears distinct from either traditional fast or slow inactivation (Milescu et al., 2010; Goldfarb, 2012). This has been termed "long-term inactivation" (Dover et al., 2010; Barbosa and Cummins, 2016), which is distinguished from conventional fast inactivation by its relatively slower recovery from inactivation and is distinguished from slow inactivation by a rate of inactivation onset comparable to traditional fast inactivation. Long-term inactivation can be mediated by regulatory proteins termed intracellular fibroblast growth factor homologous factors (iFGFs; Dover et al., 2010; Goldfarb, 2012; Venkatesan et al., 2014). Yet our understanding of such inactivation remains rudimentary.

Here, we present results addressing inactivation behavior of Nav current in rat adrenal chromaffin cells (CCs). Earlier results on Nav current in mouse CCs have revealed that recovery from inactivation occurs with two exponential components (Vandael et al., 2015b), and here we shown that this phenomenon in rat CCs has properties consistent with long-term inactivation. CCs offer a number of advantages over other cells for investigation of this phenomenon, including the simple spherical nature of the cells, the absence of processes, and possibly a single type of rapidly inactivating, tetrodotoxin-sensitive Na current (Lou et al., 2003; Vandael et al., 2015b). In both mouse and rat CCs, Nav current availability has been proposed to impact on regulation of AP firing frequency (Solaro et al., 1995; Lingle et al., 1996) and slow-wave burst firing (Vandael et al., 2015b). Mouse and rat CCs fire APs in response to constant current injection at frequencies that rarely exceed 10–20 Hz (Solaro et al., 1995; Martinez-Espinosa et al., 2014). During such sustained depolarizing current injection, CCs typically exhibit a progressive decline in AP frequency or accommodation, in some cases leading eventually to block of AP firing. Although multiple factors (Lingle et al., 2018) may contribute to accommodation in CCs, including Ca^{2+}-dependent, voltage-independent, small conductance K^+ (SK-type) channels (Vandael et al., 2012) or properties of Ca^{2+}- and voltage-dependent, large conductance K^+ (BK-type) channels (Solaro et al., 1995; Martinez-Espinosa et al., 2014), use-dependent changes in Nav availability may also contribute. Careful definition of the properties of inactivation of rodent CC Nav current and its use-dependent alteration may therefore provide new insight into the role of Nav current in CC excitability.

Here, we provide more detailed demonstration that Nav current in rat CCs exhibits two distinct components of recovery from fast inactivation, with both components entered at comparable rates during brief depolarizations. The two components differ by an order of magnitude in the rate of recovery from inactivation. There is little equilibration between pathways once inactivation has occurred. Because rates of recovery differ between the two pathways, during repetitive stimuli, channels exhibit use-dependent accumulation in the slower recovery pathway. This dual-pathway, fast inactivation mechanism appears similar to that proposed to underlie inactivation mediated by the A-isoform N termini of iFGFs for Nav current in both hippocampal Purkinje cells (Venkatesan et al., 2014) and cerebellar granule cells (Goldfarb et al., 2007). The involvement of an iFGF is confirmed in mouse CCs in the companion paper (Martinez-Espinosa et al., 2021).

Materials and methods

Animals

Sprague-Dawley rats were obtained from Harlan Laboratories or The Jackson Laboratory. Rats were sacrificed by CO_2 inhalation, following protocols approved by the Washington University in St. Louis Institutional Care and Use Committee. Following delivery of rats, animals were housed briefly in accordance with the National Institutes of Health Committee on Laboratory Animal Resources guidelines.

Adrenal slice preparation

Adrenal glands from 8–12-wk-old rats were immediately removed following euthanasia and decapitation and immersed in ice-cold Ca^{2+}- and Mg^{2+}-free Locke's buffer. Excess fat was trimmed from the glands, which were then embedded in 3% low gelling point agarose as described (Martinez-Espinosa et al., 2014). Agarose was prepared by melting agar in Locke's buffer, followed by equilibration at 37°C. After embedding of tissue, the agarose block was trimmed to ∼1-cm cubes, each containing a single gland, and then glued to a tissue stand of a vibratome (VT 1200 S; Leica). The tissue stand was then placed in a slicing chamber filled with ice-cold extracellular solution gassed with 95% O_2/5% CO_2. Glands were sectioned into 200-µm-thick slices. Slices were collected and maintained in the gassed extracellular solution at room temperature until recording. All experiments were performed within 2–6 h after slice preparation.

Slice recording methods and solutions

Recordings were done with a Multiclamp 700B (Molecular Devices). The standard extracellular solution contained (in mM) 119 NaCl, 23 $NaHCO_3$, 1.25 NaH_2PO_4, 5.4 KCl, 2.0 $MgSO_4$, 1.8 $CaCl_2$, 11 glucose, 2 sodium pyruvate, and 0.5 ascorbic acid, pH 7.4. For most voltage-clamp recordings of Nav current, the traditional open pipette, whole-cell method was used with the pipette recording solution containing (in mM) 120 CsCl, 10 NaCl, 2 $MgCl_2$, 5 EGTA, 1 Mg-ATP, and 10 HEPES (pH 7.4 with CsOH). For open pipette experiments, 90% series resistance compensation was typically employed.

Typical membrane capacitance for rat CCs included in this study was 9.0 ± 0.41 pF. Pipette resistances ranged from 1.5 to 2.5 MΩ. Electrodes were coated with Sylgard 184 (Dow Chemical). Nominal voltages are uncorrected for series resistance errors.

Dissociated cell preparations and recording methods

Methods for isolation and long-term maintenance of CCs were as described (Neely and Lingle, 1992; Herrington et al., 1995)

following methods developed by others (Kilpatrick et al., 1980; Role and Perlman, 1980; Livett, 1984). Such dissociated CCs were maintained in culture for 2–5 d.

Dissociated cells were used for perforated-patch recordings (Horn and Marty, 1988), in which spontaneous or evoked APs were recorded under current clamp and then the recorded AP waveforms were used as voltage-clamp commands. In perforated-patch recordings, for recording of APs, the pipette solution contained the following: 120 mM K-aspartate, 30 mM KCl, 10 mM HEPES (H^+), and 2 mM $MgCl_2$, adjusted to pH 7.4 with N-methylglucamine (Herrington et al., 1995). For monitoring of AP-clamp evoked inward current, 20 mM KCl was replaced by equimolar CsCl in the pipette solution. Amphotericin B (Rae et al., 1991) and pluronic acid, stored in stock solutions of dimethylsulfoxide, were added to the pipette saline to make final concentrations of 500 µg/ml. The extracellular solution for such experiments was a standard physiological solution containing (in mM) 150 NaCl, 5.4 KCl, 2 $CaCl_2$, 1 $MgCl_2$, and 5 HEPES, adjusted to pH 7.4. Recordings from dissociated cells were done with an Axoclamp 2A amplifier (Molecular Devices).

Solution exchange methods

Perfusion of external salines for dissociated cells was performed with a pipette with a single opening packed with six PE-10 internal perfusion lines, each under independent flow control (Herrington et al., 1995; Solaro et al., 1995). For adrenal slices, solution exchange was controlled from a single-bore tube entering the slice chamber. All experiments were at room temperature (21–24°C).

Data treatment and analysis

Voltage and current clamp commands and data acquisition were controlled with the Clampex program from the pClamp9 software package (Molecular Devices). Fitting of exponential relaxations and other functions was done with a nonlinear least squares procedure using the Levenberg–Marquardt algorithm or in some cases with function-fitting procedures in Excel (Microsoft). Statistical comparisons employed either a Student's *t* test or a Kolmogorov–Smirnov test. Summary data are reported either as the mean ± SD of some number of individual cells (*N*), or, when averaged data are fit to a function, the value for the fitted parameter along with 90% confidence limit of that fitted parameter is provided. For Boltzmann fits of steady-state current availability, the following equation was used: $\left\{\frac{I(V)}{I_{max}} = 1/\left[1 + exp^{\frac{zF(V-V_{0.5})}{RT}}\right]\right\}$, where I(V) / I(max) reflects the fraction of maximal current available at a given conditioning potential, F/RT have their usual physical chemical meanings, with z reflecting the voltage-dependence of the distribution of channels between available and inactivated states, V representing the conditioning potential, and $V_{0.5}$ the voltage at which half the channel population is inactivated. The Boltzmann equation to fit activation G-V curves was $\left\{\frac{G(V)}{G_{max}} = 1/\left[1 + exp^{\frac{zF(V-V_{0.5})}{RT}}\right]\right\}$, where z reflects the voltage-dependence of the channel activation equilibrium and $V_{0.5}$ is the voltage at which half the maximal conductance is activated, with the other parameters as above. It should be noted that this is an empirical description of sodium channel activation since the rapid inactivation of Nav current precludes precise definition of the voltage-dependence of channel activation at a given voltage.

Online supplemental material

Fig. S1 shows predicted state occupancies and peak current decrement during trains of different frequencies. Fig. S2 shows calculated fractional occupancies of fast and slow recovery pathways during AP clamp waveform trains.

Results

Basic properties of Nav current from CCs in rat adrenal medullary slices

Fig. 1 A shows a series of superimposed voltage-clamp records during 5-ms depolarizing steps of increasing amplitude following a 1,000-ms step to −120 mV. Steps ranged from −70 mV to +50 mV in 5-mV increments (only 10-mV increments are displayed). Average peak current for 18 cells versus command potential is plotted in Fig. 1 B with peak sodium current (I_{Na}) near −15 mV. Average peak inward Nav current was −9,494 ± 2,600 pA (mean ± SD) corresponding to an average peak current density of −1,067 pA/pF, which is several-fold larger than previously described for bovine (Fenwick et al., 1982) and mouse (Vandael et al., 2015b) CCs. Assuming a +66 mV reversal potential, the normalized conductance-versus-voltage (G/V) curves (Fig. 1 C) for this set of cells yielded a voltage of half activation ($V_{0.5}$) of −27.4 ± 0.2 mV with $z = 5.4 \pm 0.2e$. This $V_{0.5}$ is within ∼5 mV of values reported for Nav current in rat sympathetic neurons (Belluzzi and Sacchi, 1986; Schofield and Ikeda, 1988) and mouse CCs (Vandael et al., 2015b). The rate of onset of inactivation, measured from single exponential fits to the decay phase of the Nav current, was voltage-dependent with the time constant varying from ∼2 ms at −25 mV, approaching 0.3 ms near 30 mV (Fig. 1 D).

In bovine CCs, the voltage at which Nav channels are half inactivated ($V_{0.5}$) at steady-state was reported to be −34 mV using 25-ms conditioning steps (Fenwick et al., 1982). In contrast, one study of rat CCs, using a 250-ms conditioning step, reported a $V_{0.5}$ for steady-state inactivation of −60 mV (Hollins and Ikeda, 1996), while another reported a $V_{0.5}$ of −62 mV with a 500-ms prepulse duration (Lou et al., 2003). Here, we examined the effect of conditioning duration on the $V_{0.5}$ of inactivation. With a 25-ms conditioning step, $V_{0.5}$ = −35.4 mV (Fig. 1, E and F), similar to that reported for bovine CCs (Fenwick et al., 1982). Steady-state inactivation curves shifted considerably to more negative voltages as the duration of the conditioning step increased from 25 ms up to 1 s (Fig. 1 E), with a $V_{0.5}$ for steady-state inactivation of −57.7 mV with a 1-s conditioning step (Fig. 1 F). The modest change in $V_{0.5}$ between 500 ms and 1 s suggests that a conditioning step of 1 s is sufficient to approach a steady-state $V_{0.5}$ of Nav availability in rat CCs.

Recovery from inactivation occurs with both fast and slow components

Temporal features of recovery from inactivation were examined using standard paired depolarizing pulses to 0 mV (Fig. 2 A) separated by recovery periods of varying length at a given

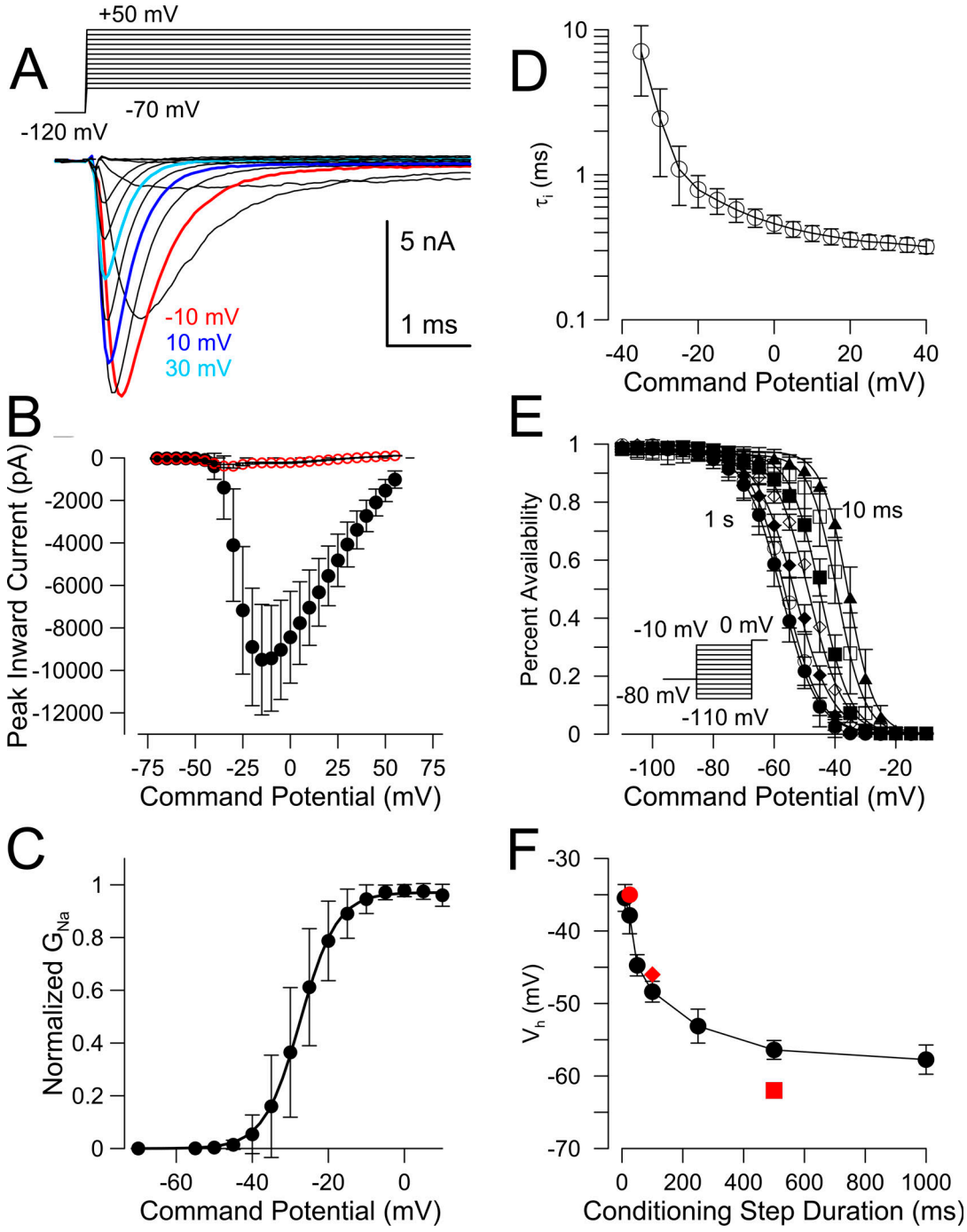

Figure 1. **Basic properties of Nav current and steady-state inactivation in rat CCs. (A)** Nav current was activated with the indicated stimulus protocol in a rat adrenal CC in a slice. **(B)** The averaged peak-current density for inward current is plotted (mean ± SD) for a set of 18 rat CCs. The steady-state current (at end of 5-ms step) for the same set of cells is shown in red. **(C)** Currents from the set of patches in B were used to generate a G/V curve (mean ± SD), assuming E_{Na}= 66 mV. For each cell, extrapolation of currents activated at +50 and +55 mV yielded E_{Na} = 64.4 ± 2.9 mV (mean ± SD), while E_{Na} calculated from nominal intracellular and extracellular solutions was 67 mV. The fitted voltage of half activation was −27.4 ± 0.2 mV with z = 5.4 ± 0.2*e*. **(D)** The rates (mean ± SD; *n* = 12 cells) of onset of inactivation measured from single exponential fits to the decay phase of the Nav currents are plotted as a function of the inactivation voltages. **(E)** Fractional availability (mean ± SD) is plotted as a function of conditioning potential over a range of conditioning potential durations (10, 25, 50, 100, 250, 500, and 1,000 ms). Inset shows example voltage protocol, where conditioning potential ranged from −110 to −10 mV (5-mV increments), with a test potential of 0 mV, following an initial holding potential of −80 mV. Numbers of patches tested for each recovery voltage were, from 10 to 1,000 ms, 8, 4, 6, 9, 6, 7, and 13. $V_{0.5}$ and *z* for single Boltzman fits were, for 10 ms, −35.6 ± 0.3 mV, *z* = 5.9 ± 0.3*e*; for 25 ms, $V_{0.5}$ = −39.2 ± 0.4 mV, *z* = 5.7 ± 0.4*e*; for 50 ms, $V_{0.5}$ = −44.8 ± 0.4 mV, *z* = 5.1 ± 0.4*e*; for 100 ms, $V_{0.5}$ = −48.7 ± 0.5 mV, *z* = 4.5 ± 0.3*e*; for 250 ms, $V_{0.5}$ = −53.2 ± 0.4 mV, *z* = 4.1 ± 0.2*e*; for 500 ms, $V_{0.5}$ = −56.5 ± 0.3 mV, *z* = 4.4 ± 0.2; and for 1,000 ms, $V_{0.5}$ = −57.7 ± 0.2 mV, *z* = 4.3 ± 0.1*e*. **(F)** The mean $V_{0.5}$ of fractional availability obtained from single Boltzman fits to the curves from each individual cell used for the averages in E is plotted (±SD; *n* = 4–13 cells, as indicated) as a function of conditioning potential duration. The line simply connects the dots. Red symbols correspond to measurements of voltage of half availability in previous papers with different conditioning step durations (circle: bovine CCs, Fenwick et al. [1982]; diamond: rat CCs, Hollins and Ikeda [1996]; square, rat CCs, Lou et al. [2003]).

recovery potential. An initial holding potential of −80 mV, at which more than 95% of the Nav channels are available for activation (Fig. 1 E), preceded the first test pulse. I_{Na} amplitude during the second depolarizing pulse (P2) following each recovery interval was normalized to I_{Na} activated during pulse 1. Example currents evoked from the paired pulse stimulation protocol (1 ms to 3 s recovery) are shown in Fig. 2, A and B, with recovery either at −60 mV (Fig. 2 A) or −120 mV (Fig. 2 B). Over a range of recovery potentials (−60 to −120 mV), the fractional recovery as a function of recovery duration is not well-described by a single exponential time course (Fig. 2 C), while a double exponential provides an excellent fit (Fig. 2 D). The double exponential nature of the recovery time course can be best seen by plotting the recovery durations on a logarithmic time scale (right panels of Fig. 2, C and D).

The averaged fractional recovery and associated standard errors were plotted along with the best fit of the double exponential function for one set of cells studied at recovery potentials of −50, −70, −90, and −110 mV (Fig. 3 A) and another set of cells at −60, −80, −100, and −120 mV (Fig. 3 B). Over the tested recovery voltages, the faster time constant of recovery ranged from ∼55.9 ± 1.1 ms at −60 mV to 2.9 ± 0.4 ms at −120 mV, while the slower time constant plateaued at 487 ± 8 ms at −60 mV, and was around 56.5 ± 0.6 ms at −120 mV (Fig. 3 C). A plot of the relative amplitude of each recovery component as a function of voltage shows that, at potentials negative to about −80 mV, most inactivated channels fully recover from inactivation (Fig. 3 D). However, at more positive recovery potentials, the relative amplitudes of the slow and fast recovery components exhibit some differences. Thus, with recovery at −70 mV, the absolute amplitude of the slow recovery (A_s) process is similar to that at the most negative recovery potentials, but the amplitude of the fast recovery (A_f) component is reduced. Minimally, the results indicate that multiple inactivated states participate in the recovery process, but interpretation of the significance of the slow and fast recovery components depends on the relationship among inactivated states. For the moment, we propose that the two components reflect largely separate and independent inactivation pathways, and we test this further below.

Empirically, the fraction of channels recovering either through slow or fast pathways as a function of recovery potential can each be fit with a single Boltzmann function. For the fast recovery component, $V_{0.5}$ is −61.8 ± 1.5 mV (z = 3.1 ± 0.8e), whereas for the slow recovery component, the $V_{0.5}$ is −57.3 ± 0.9 mV (z = 6.2 ± 1.9e). When the amplitudes of both recovery components are added together, reflecting the full fractional recovery at each recovery potential, the summed amplitudes can be well fit with a single Boltzmann with $V_{0.5}$ = −58.6 ± 0.3 mV with z = 3.7 ± 0.2e, agreeing closely with the steady-state inactivation curves measured following a 1-s conditioning potential (Fig. 1 E).

Although we have not examined this in detail, we did observe some cells for which the relative amplitudes of the fast and slow components of recovery were not as similar as for the cells in Fig. 3 (e.g., Figs. 4 and 5). We have no definitive answer for such differences in A_f and A_s. Possible explanations might include (1) differential expression of two populations of Nav channels and (2) differential contribution of some molecular component that contributes to the slower component of recovery from inactivation. We consider the latter possibility more likely (Martinez-Espinosa et al., 2021).

Models of slow recovery from inactivation

To guide consideration of the experiments presented below, we begin with two general categories of scheme by which multiple components of recovery from inactivation might occur. Scheme 1 encapsulates a traditional view of slow inactivation (Zhang et al., 2013; Silva, 2014) in which there are two tiers of inactivated states, one (I_1–I_6) in which recovery from inactivation is fast, and another (I_1'–I_6') in which return to other states is slow. Thus, occupancy of more slow recovering states occurs sequentially from occupation of fast recovering states. More recent work suggests that movement of the Domain IV (DIV) voltage sensor of Nav1.4 is rate limiting for fast inactivation (Capes et al., 2013), but for present purposes, Scheme 1 encapsulates a general model in which traditional slow inactivation is linked to entry into fast inactivated states.

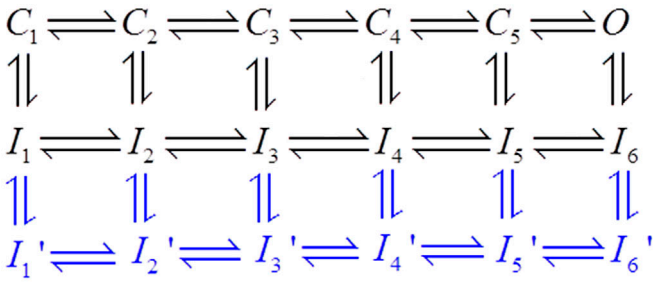

(Scheme 1)

Scheme 1 requires that entry into states from which recovery occurs slowly depends first on entry into the fast recovery states. A characteristic of such a scheme is that, as the duration of the inactivation step is increased, the amplitude of any slow component of recovery will increase (Zhang et al., 2013; Silva, 2014). It should be noted immediately that the observation in CCs that both slow and fast components of recovery of about equal amplitude are observed following a 5-ms depolarization is inconsistent with Scheme 1, unless entry into I_1'–I_6' is very rapid.

A second general model has been proposed to explain the effects of iFGFs on slow recovery from inactivation of particular Nav currents in neurons (Goldfarb et al., 2007; Dover et al., 2010; Milescu et al., 2010; Goldfarb, 2012; Venkatesan et al., 2014). Scheme 2 posits two distinct fast inactivation pathways, one identical to conventional fast inactivation (I_1–I_6), while the other involves a competing fast inactivation pathway into states that recover more slowly from inactivation (I_{SR}). Scheme 2 also includes traditional slow inactivation states. As schematized in Scheme 2, the secondary fast inactivation pathway only occurs from the open state, but this is only for illustrative purposes, and this category of mechanism might also permit inactivation from some number of closed states (Milescu et al., 2010; Venkatesan et al., 2014). An important idea encapsulated in Scheme 2 that distinguishes it from Scheme 1 is that entry into I_{SR} is essentially competitive with normal fast inactivation, under conditions that

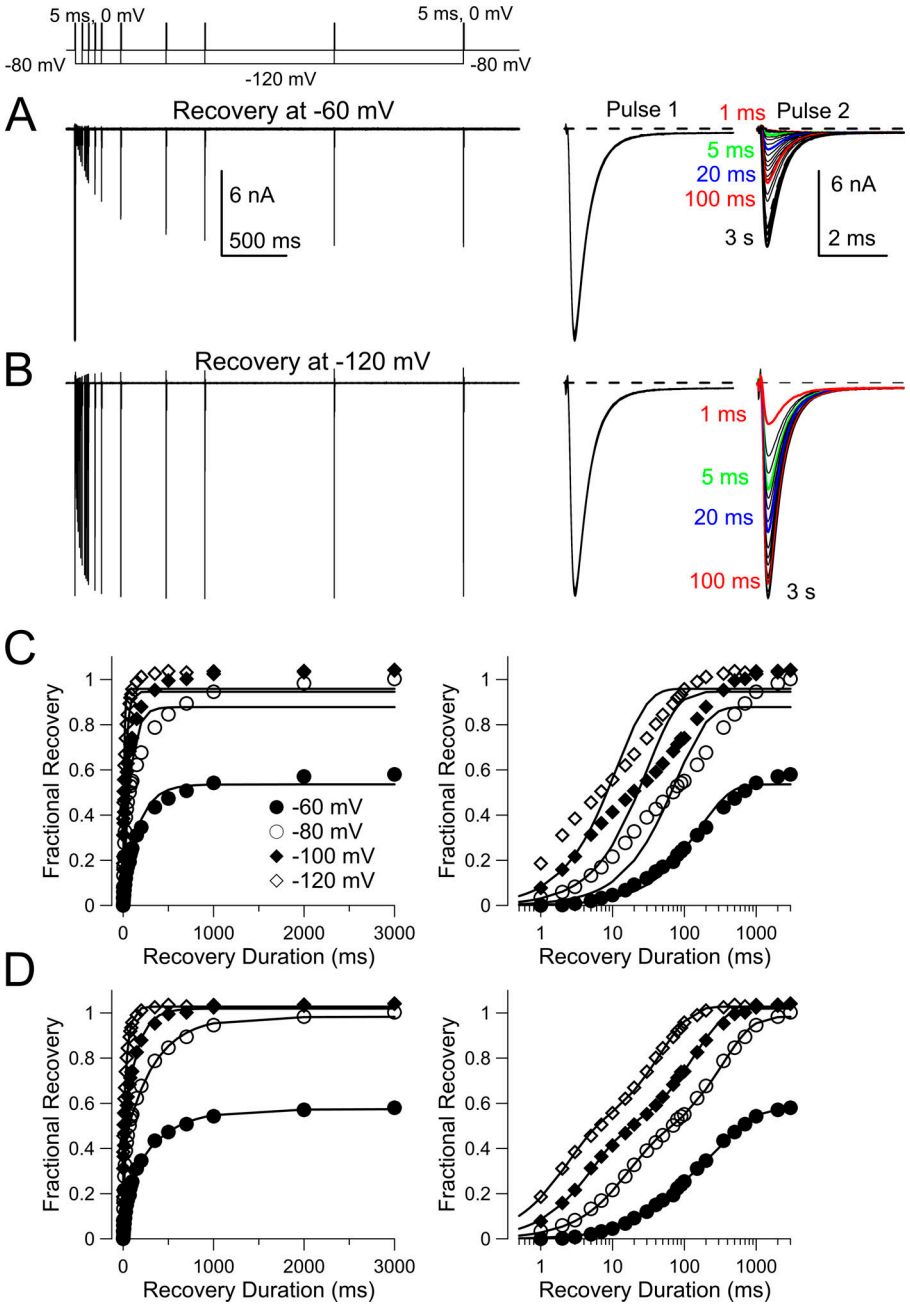

Figure 2. **Recovery from fast inactivation involves two components.** A paired pulse protocol (top) was used to examine the time course of recovery from inactivation. From a holding potential of −80 mV, a 5-ms activation step to 0 mV was used to produce Nav inactivation. In a given trial, the cell was then repolarized to a voltage between −60 and −120 mV for durations from 1 ms to 3 s before the second test step to 0 mV. The example protocol (top) shows example paired-pulse intervals for 50, 100, 200, 350, 700, 1,000, 2,000, and 3,000 ms recovery intervals at −120 mV. **(A)** A family of traces showing recovery from inactivation at −60 mV. On the right, traces are shown for the response to the initial step to 0 mV (pulse 1) and then for the response to the second step to 0 mV (pulse 2) following the recovery step. Colored traces highlight recovery at the indicated intervals. **(B)** As in A, traces are shown for recovery at −120 mV. **(C)** Fractional recovery from 1 ms to 3 s is plotted for recovery at −60, −80, −100, and −120 mV for the cell shown in A and B using a linear scale on the left and a logarithmic scale on the right. Lines are fits of a single exponential function to the recovery time course: $I_t = A[1 - exp(-t/\tau)]$, where A and τ are the amplitude and time constant of the recovery process, respectively. **(D)** The same fractional recoveries shown in C are replotted along with fits of a double exponential function to the recovery time course with $I_t = A_f[1 - \exp(-t/\tau_f)] + A_s[1 - \exp(-t/\tau_s)]$, where A_f and A_s are amplitudes of fast and slow recovery components, respectively, and τ_f and τ_s are the respective time constants of fast and slow recovery. For −60 mV, A_f = 0.19 ± 0.03, τ_f = 49.9 ± 7.9 ms, A_s = 0.38 ± 0.02, and τ_s = 373.7 ± 34.6 ms (fitted value and 90% confidence limit). For −80 mV, A_f = 0.40 ± 0.01, τ_f = 14.8 ± 0.9 ms, A_s = 0.59 ± 0.01, and τ_s = 332.0 ± 19.7 ms. For −100 mV, A_f = 0.44 ± 0.01, τ_f = 5.0 ± 0.4 ms, A_s = 0.58 ± 0.1, and τ_s = 134.7 ± 8.4 ms. For −120 mV, A_f = 0.46 ± 0.01, τ_f = 2.1 ± 0.1 ms, A_s = 0.57 ± 0.01, and τ_s = 46.1 ± 2.4 ms.

favor channel opening. Conceivably, other mechanisms might allow the possibility of transitions between the two distinct inactivation pathways, e.g., between I_{SR} and I_6.

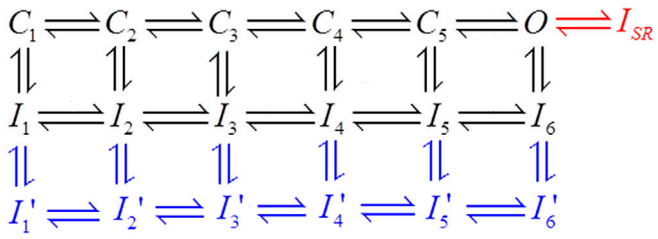

(Scheme 2)

Although both Schemes 1 and 2 are consistent with currents that exhibit both slow and fast components of recovery from inactivation, Schemes 1 and 2 make qualitatively very different predictions for the properties of entry and recovery from inactivation. We now use a set of protocols to show that inactivation of Nav current in rat CCs exhibits a behavior consistent with Scheme 2, but not Scheme 1. The basic approach is to use protocols that, beginning from some specific initial condition, e.g., channels in resting states or channels in some condition of steady-state inactivation, then allow determination of the time course of either recovery from inactivation or onset of inactivation, in order to try to tease apart the connectedness between states underlying the two observed inactivation time constants.

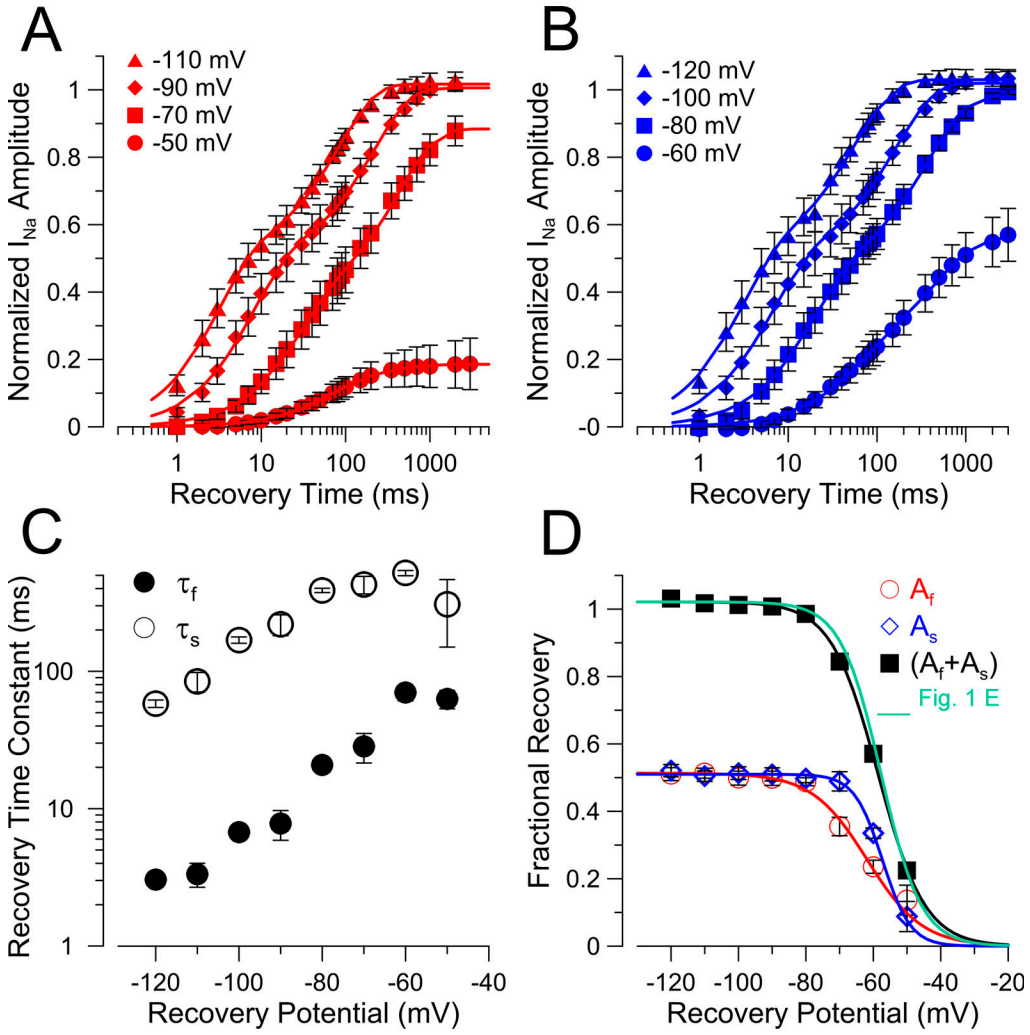

Figure 3. **Voltage-dependence of two components of recovery from inactivation. (A)** A log-scale plot of averaged fractional recovery from inactivation following a 5-ms depolarizing voltage step to 0 mV is shown for recovery voltages of −50, −70, −90, and −110 mV, using the protocol illustrated in Fig. 2. Each point shows the mean ± SD (at −50 mV, *n* = 11 cells; at −70, *n* = 14; at −90, *n* = 15; and at −110 mV, *n* = 13). Lines are the best fit of a two-exponential function to the recovery time course. Each cell was equilibrated at −80 mV for 1 s before the initial inactivating test step to 0 mV. At −110 mV, A_f = 0.51 ± 0.01, τ_f = 3.1 ± 0.2 ms, A_s = 0.51 ± 0.01, and τ_s = 83.2 ± 4.7 ms (fitted value and 90% confidence limit); at −90 mV, A_f = 0.50 ± 0.01, τ_f = 7.6 ± 0.5 ms, A_s = 0.51 ± 0.01, and τ_s = 215.3 ± 17.1 ms; at −70 mV, A_f = 0.36 ± 0.01, τ_f = 23.1 ± 1.6 ms, A_s = 0.53 ± 0.13, and τ_s = 404.9 ± 27.3 ms; for −50 mV, A_f = 0.14 ± 0.01, τ_f = 64.7 ± 5.8 ms, A_s = 0.05 ± 0.01, and τ_s = 359.1 ± 110.9 ms. **(B)** For a different set of cells (10 or 11 cells), fractional recovery was determined at −60, −80, −100, and −120 mV, with solid lines indicating the double exponential fit. At −120 mV, A_f = 0.51 ± 0.01, τ_f = 2.9 ± 0.4 ms, A_s = 0.52 ± 0.01, and τ_s = 56.5 ± 0.6 ms; at −100 mV, A_f = 0.50 ± 0.01, τ_f = 6.4 ± 0.6 ms, A_s = 0.53 ± 0.01, and τ_s = 162.9 ± 1.8 ms; at −80 mV, A_f = 0.45 ± 0.01, τ_f = 18.4 ± 0.3 ms, A_s = 0.53 ± 0.01, and τ_s = 373.5 ± 6.1 ms; at −60 mV, A_f = 0.21 ± 0.01, τ_f = 55.93 ± 1.1 ms, A_s = 0.34 ± 0.01, and τ_s = 487.8 ± 7.6 ms. **(C)** At each recovery voltage, the mean fast and slow time constants (±SD) obtained from fits to individual cells are plotted for each set of cells. These mean values for sets of individual cells agree closely with the fits to the averaged data shown in A and B. **(D)** The mean amplitude (±SD) of faster and slower recovery components are plotted as a function of voltage along with the sum of the two components. Single Boltzmann fits to each relationship are shown. For the fast component (red circles), A_f = 0.51 ± 0.02, $V_{0.5}$ = −61.8 ± 1.5 mV, and *z* = 3.2 ± 0.8*e*; for the slow component (blue circles), A_s = 0.51 ± 0.01, $V_{0.5}$ = −57.3 ± 0.87 mV, and *z* = 6.2 ± 1.9*e*. For the sum of the two components (black rectangles), $V_{0.5}$ = −58.6 ± 0.3 mV with *z* = 3.7 ± 0.2*e*, agreeing closely with the measurements of fractional availability in Fig. 1 E (green line), $V_{0.5}$ = −57.7 mV and *z* = 4.3*e*.

The duration of depolarizing steps does not strongly influence distribution between slow and fast recovery paths

For traditional slow inactivation, as the duration of a strong inactivating depolarization is increased, the relative A_s from inactivation gradually increases (Zhang et al., 2013; Silva, 2014). At first glance, the fact that both fast and slower recovery from inactivation occurs with comparable fractional amplitudes after even a 5-ms depolarizing step tends to argue against Scheme 1, i.e., traditional slow inactivation. To examine this more closely, we determined the relative amplitude and rates of fast and slow recovery from inactivation using paired pulses to +0 mV, but with depolarizing step durations of 5, 25, 100, 250, and 500 ms (Fig. 4, A–E). The recovery time courses from one cell show that, as the duration of the inactivation step is increased, there is some decrement in the A_f component at longer depolarizations (compare Fig. 4 A to Fig. 4, C and D). Plotting the fractional recoveries for a set of 16 cells tested at 5, 25, 100, and 250 ms for which 10 of the cells were also tested at 500 ms showed a

consistent small decrement in the fast component (Fig. 4 E) and some slowing of both τ_f and τ_s, the fast and slow time constants of recovery, respectively. Because of concern that the sequence of the pulse protocols might result in some slow change in channel behavior, we also used a reverse sequence of inactivation durations of 500, 250, 100, 25, and 5 ms in a set of four cells and obtained similar changes in the amplitudes and durations of recovery components with longer inactivation durations (plotted in Fig. 4 G). Longer depolarizing step durations (500 and 1,000 ms) were explored in another set of four cells (Fig. 4 F). The changes in A_f and A_s components were plotted as a function of the depolarizing step duration (Fig. 4 G) and fit with a single exponential function, indicating that the decrement in A_f occurred with a time constant of 248 ± 126 ms approaching steady-state at a fractional amplitude of 0.26 ± 0.3, while the increase in A_s occurred with a similar time constant of 219 ± 205 ms and limiting steady-state amplitude of 0.72 ± 0.02. Both the fast and slow recovery time constants were slightly slowed with longer depolarizing step durations (Fig. 4 H). Whatever the origin of the changes in the properties of the fast and slow recovery components, they occur with time constants much slower than the initial rapid rates of entry into the two recovery pathways. Overall, the results indicate that, once channels have distributed about equally between the two recovery pathways after a 5-ms depolarization, there is only a small additional change in relative fractions of fast and slower recovering channels up through 100 ms at the depolarizing voltage.

What might be the origin of the small change in ratio of fast and slow components of recovery with more prolonged depolarizing pulses? Although it is possible there is some additional equilibration between the two pathways after the initial fast inactivation, another possibility is that it might simply reflect a small contribution of something akin to traditional slow inactivation (Zhang et al., 2013; Silva, 2014). For Nav1.5, a tetrodotoxin-resistant cardiac Nav channel for which some quantitative estimates of slow inactivation are available (Zhang et al., 2013), entry into slow inactivation at −20 mV was observed to occur with a time constant of 1.8 s, with slow inactivation only beginning to be detectable with depolarizations of 100 or 200 ms. Recovery from slow inactivation for Nav1.5 occurs with time constants on the order of hundreds of milliseconds at −120 mV. The onset of Nav1.5 slow inactivation is slower than what we observe here for the additional slow equilibration of the CC Nav currents. However, overall, the slow changes in the amplitudes of both the slow and fast components and the prolongations in the time constants are generally consistent with what would be expected if channels were entering an additional slow recovery state. However, the present results do not provide any definitive insight into this issue.

The relatively unchanged amplitudes of slow and fast recovery components over 100 ms of inactivation seems generally more compatible with Scheme 2 than Scheme 1. However, Scheme 1 could apply under the condition that equilibration between the two tiers of inactivated states in Scheme 1 has to be complete within 5 ms and not change substantially change over 100 ms. If so, that would be a highly unusual form of traditional slow inactivation.

Relative entry into slow and fast recovery paths exhibits little voltage dependence

We next examined whether the voltage at which channels inactivate might affect relative entry into the two pathways. We focused on voltages over which activation of Nav current was near saturation (Fig. 1 C) such that any differences would be expected to largely reflect intrinsic voltage dependence in transitions involved in inactivation. Recovery at −80 mV was examined following inactivation produced by a 25-ms step at command voltages from −10 to +30 mV (Fig. 5 A). A 25-ms depolarization was chosen since inactivation is essentially complete within this time period over these voltages. With depolarizations from −10 to +30 mV, there is little change in the time course of recovery from inactivation (Fig. 5, A and B). For a set of >10 cells, the amplitude of the fast component was slightly diminished at −10 mV but essentially constant from 0 to 30 mV (Fig. 5, C and D). The voltages over which the relative amplitudes of the two recovery components are voltage-independent corresponds approximately to voltages over which Nav conductance is maximally activated (Fig. 1 C). This indicates that there is little intrinsic differential voltage dependence of entry into inactivated states, i.e., relative amplitudes of fast and slow recovery remain constant, and, furthermore, rates of recovery are not affected by the voltage at which inactivation occurred (Fig. 5 D). Although this protocol per se does not fully distinguish between a Scheme 1 or Scheme 2 type of inactivation, the results suggest that changes in voltage do not alter the distribution among states leading to fast and slow recovery.

To further test whether any manipulations might alter the distribution of channels among different recovery pathways, we used a protocol in which recovery following inactivation produced by a 5-ms step to 0 mV was examined either with or without a subsequent 50-ms depolarization to +70 mV just preceding the recovery period (Fig. 6, A and B). Similar to the impact of increasing duration of depolarizations (Fig. 4), once inactivation has occurred, an additional 50-ms depolarization to +70 mV produces only a modest reduction in the fraction of channels that recover through the fast pathway (Fig. 6, C–E). Any additional reduction in the fraction of channels that recover through the fast pathway is generally consistent with the reduction that is observed for increases in inactivation step duration from 5 ms to 55 ms at 0 mV (Fig. 4 G). Thus, once inactivation has occurred, there is little change in the relative ratio of channels in each recovery pathway.

Based on the idea that traditional slow inactivation involves slow entry from fast inactivated states Scheme 1, the results in Figs. 4, 5, and 6 seem more compatible with a scheme involving entry into two separable fast inactivation pathways Scheme 2. Scheme 1 could only be applicable if rates of conversion between fast and slow recovery states were very rapid at positive voltages. This seems unlikely, since at least over voltages from −120 to −50 mV, exit from the slow recovery pathway is ∼10-fold slower than for fast recovery (Fig. 3 C).

Accumulation of channels in slow recovery paths during repetitive depolarizing steps requires two independent inactivation pathways

A prediction that arises from the idea that there are two independent, nonequilibrating recovery pathways for CC Nav current inactivation is that sequential inactivation steps with short recovery times should produce a use-dependent accumulation of

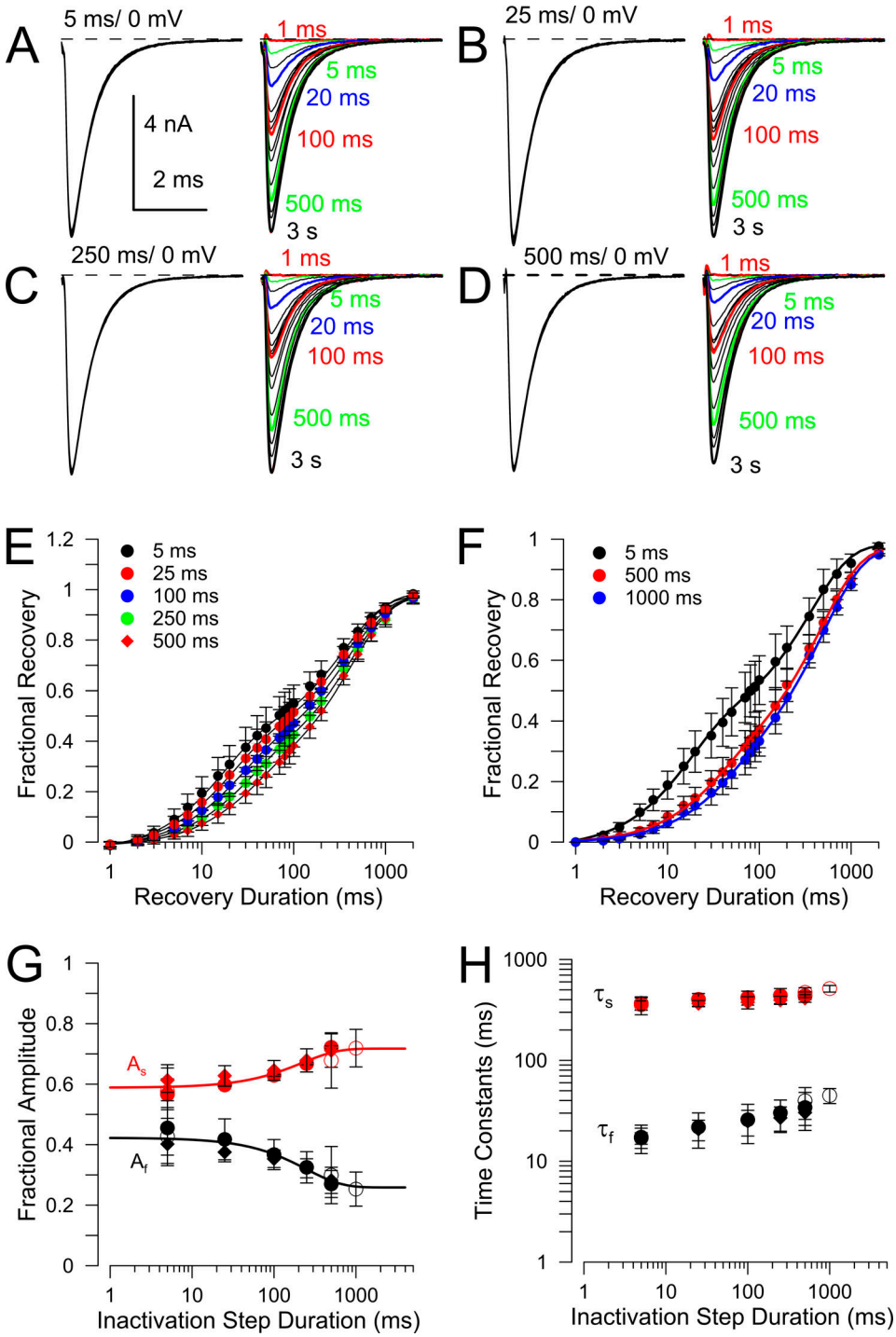

Figure 4. **Effects of variation in duration of inactivation step on relative amplitudes of fast and slow components. (A–D)** Paired depolarizing pulses to +0 mV from a −80-mV holding potential were used to examine the time course of recovery from inactivation with inactivation pulse durations of 5, 25, 250, and 500 ms duration. All traces are from the same cell, with colored traces showing recovery durations preceding the second pulse indicated on each panel. **(E)** Mean fractional recovery (16 cells for 5, 25, 100, and 250 ms, and 10 cells for 500 ms) following the indicated inactivation durations are plotted as a function of recovery duration, with each set of points fit by a double exponential recovery function. Errors bars in E and F are SD. For 5 ms inactivation, A_f = 0.44 ± 0.01, τ_f = 16.2 ± 1.12 ms, A_s = 0.57 ± 0.01, and τ_s = 359.4 ± 21.3 ms; for 25 ms, A_f = 0.41 ± 0.01, τ_f = 19.4 ± 1.5 ms, A_s = 0.60 ± 0.01, and τ_s = 389.9 ± 22.2 ms; for 100 ms, A_f = 0.36 ± 0.01, τ_f = 22.7 ± 1.8 ms, A_s = 0.63 ± 0.01, and τ_s = 404.6 ± 20.3 ms; for 250 ms, A_f = 0.32 ± 0.02, τ_f = 27.9 ± 3.1 ms, A_s = 0.68 ± 0.02, and τ_s = 430.3 ± 24.7 ms; for 500 ms, A_f = 0.26 ± 0.01, τ_f = 31.1 ± 3.5 ms, A_s = 0.73 ± 0.01, and τ_s = 432.3 ± 18.9 ms. **(F)** Recovery was examined in another set of four cells for 5, 500, and 1,000 ms inactivation durations at 0 mV, again with double exponential fits overlaid. For 5 ms, A_f = 0.40 ± 0.01, τ_f = 16.4 ± 1.4 ms, A_s = 0.60 ± 0.01, and τ_s = 364.9 ± 22.6 ms; for 500 ms, A_f = 0.26 ± 0.02, τ_f = 34.6 ± 3.4 ms, A_s = 0.71 ± 0.01, and τ_s = 476.1 ± 23.1 ms; for 1,000 ms, A_f = 0.24 ± 0.02, τ_f = 44.5 ± 5.9 ms, A_s = 0.73 ± 0.02, and τ_s = 509.2 ± 28.9 ms. **(G)** The A_f and A_s components are plotted as a function of recovery duration. In this case, the A_f and A_s values from each individual cell in E were averaged to determine the mean ± SD. Filled circles correspond to cells tested sequentially with 5, 25, 100, 250, and 500 ms inactivation durations. Filled diamonds correspond to cells tested in the sequence of 500, 250, 100, 25, and 5 ms. Open circles correspond to four cells tested

with 5, 500, and 1,000 ms durations in both forward and reverse orders. Solid lines correspond to single exponential fits to the temporal changes in each amplitude component. Changes in A_f occur with a time constant of 248.0 ± 126.0 ms, while A_s changes with a time constant of 219.0 ± 205.1 ms. A_f, A_s, τ_f, and τ_s values measured at 5 and 25 ms were not statistically different. **(H)** The time constants for fast and slow recovery monitored at −80 mV following inactivation steps for different durations to 0 mV are plotted, illustrating a slow prolongation of both τ_f and τ_s with inactivation duration. Errors bars are SD.

channels in the slower-recovering inactivated states. Specifically, if brief recovery periods are interposed between depolarizing command steps, each recovery period would allow a larger fraction of channels in fast recovery pathways to recover than would occur through the slower pathway. Since a short recovery period selectively favors recovery of channels from fast inactivation pathways, a series of depolarizing steps will result in the accumulation of channels in the slow recovery states, but only if the pathways are separate. In contrast, if at strong depolarizations there is rapid equilibration of channels among states leading to both slow and fast recovery pathways, accumulation of channels in slow recovery pathways will not occur. We tested these alternatives in Fig. 7. We produced inactivation with a 5-ms depolarization to +0 mV, which approximates the width of a naturally occurring CC AP at 0 mV (see Fig. 10). We compared recovery from inactivation following a single depolarizing step (Fig. 7, A and D) to 0 mV to that after trains of 5 (Fig. 7 B), 10, or 20 (Fig. 7 C) inactivation steps, with 15 ms

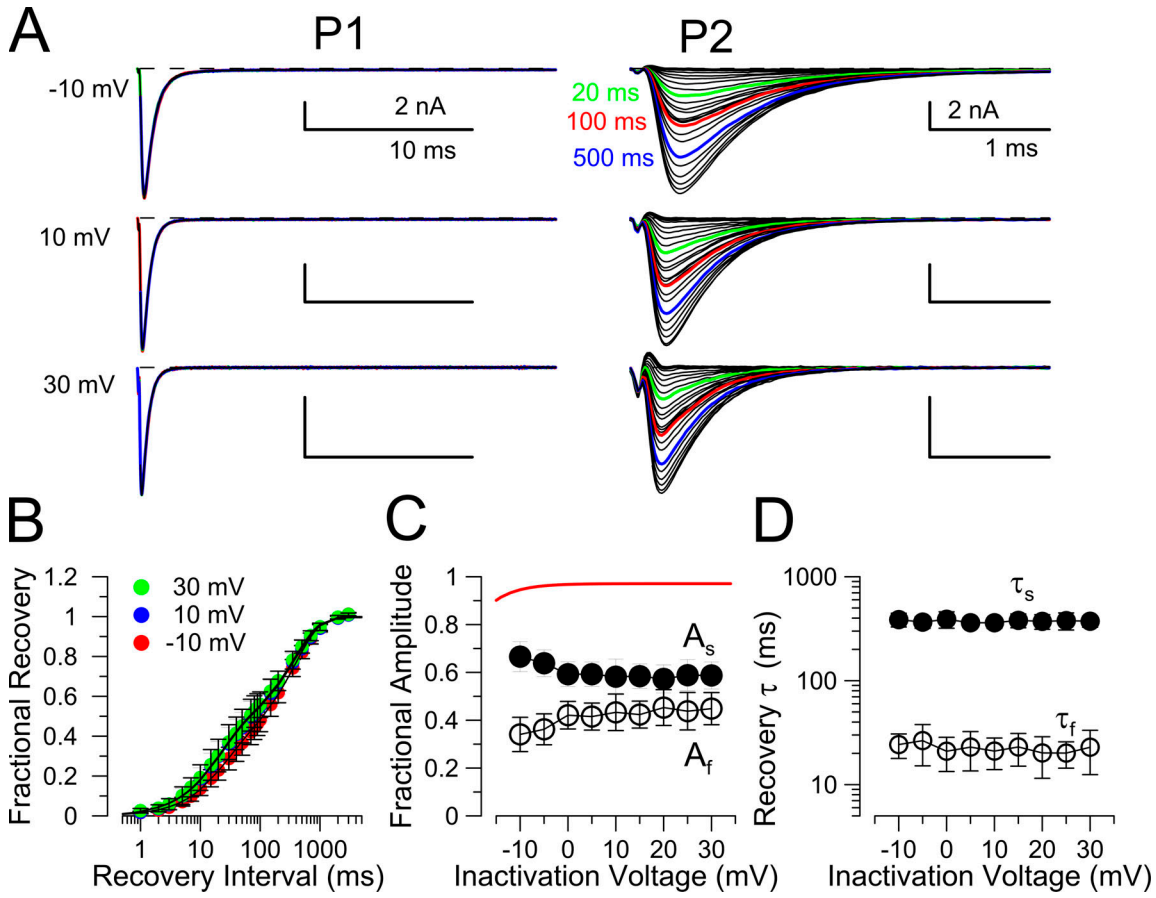

Figure 5. **Relative entry into slow and fast recovery pathways is voltage-independent above −10 mV. (A)** The standard paired pulse protocol was employed with a 25-ms inactivation depolarization (pulse 1, P1) to voltages from −10 mV to +30 mV, with recovery intervals (at −80 mV) from 1 ms to 3 s, followed by a final 5-ms test step (pulse 2, P2) to the initial inactivation voltage. Traces show currents evoked during P1 on the left for a given voltage, and then during P2 on the right. From top to bottom, traces reflect inactivation voltages of −10, 10, and +30 mV. Green, red, and blue traces show currents following recovery intervals of 20, 100, and 500 ms, respectively. Over this range of voltage, activation of Nav conductance is near maximum (Fig. 1 C). **(B)** Averaged recoveries following inactivation at the indicated voltages (−10 mV, *n* = 12 cells; 10 mV, *n* = 13 cells; +30 mV, *n* = 11 cells). Colored symbols and error bars show mean ± SD with lines reflecting best fits of a double exponential with the following parameters. Following inactivation at −10 mV, A_f = 0.33 ± 0.01, τ_f = 23.1 ± 1.3 ms, A_s = 0.67 ± 0.01, and τ_s = 372.4 ± 14.1 ms; at +10 mV, A_f = 0.42 ± 0.02, τ_f = 20.0 ± 1.1 ms, A_s = 0.58 ± 0.01, and τ_s = 376.1 ± 20.2 ms; and at +30 mV, A_f = 0.42 ± 0.01, τ_f = 19.4 ± 1.0 ms, A_s = 0.58 ± 0.01, and τ_s = 361.4 ± 19.2 ms. Note that the points for recovery at +10 mV are largely obscured by those for recovery at +30 mV. **(C)** Mean values (±SD) for the amplitudes of the fast (open black circles, A_f) and slow (filled black circles, A_s) recovery components determined from fits to recovery from at least 11 cells at each voltage are plotted as a function of different inactivation voltages. The red line corresponds to the Nav G/V curve from Fig. 1 C. **(D)** Mean values (±SD) for fast and slow recovery time constants (τ_f and τ_s) for the same set of cells are plotted as a function of the inactivation voltage.

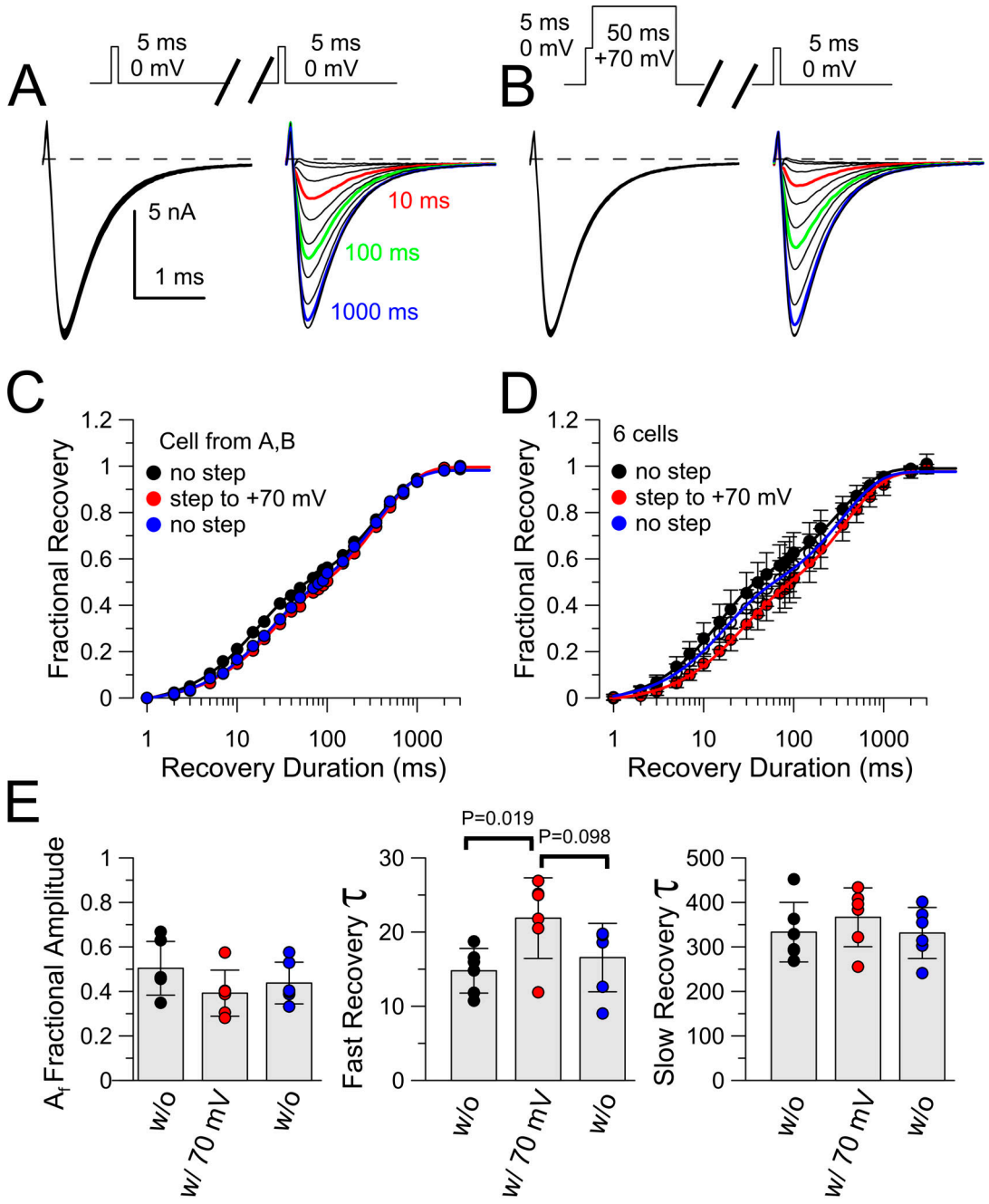

Figure 6. **Once inactivation has occurred, additional prolonged depolarization produces only minor changes in distribution between fast and slow recovery. (A)** A standard paired pulse protocol (5 ms to +0 mV) was used to examine recovery from inactivation at −80 mV with recovery in response to the second pulse shown on the right. **(B)** Following inactivation at +0 mV, a 50-ms step to +70 mV preceded the recovery step to −80 mV, with individual recovery tests on the right. **(C)** Fractional recoveries for the cell shown in A and B are plotted, along with an additional control protocol without the +70 mV step. Lines are fits of a double exponential function to the recovery time courses. With no step to +70 mV, A_f =0.46 ± 0.01 (mean ± confidence limit), τ_f = 14.8 ± 0.7 ms, A_s = 0.56 ± 0.01, and τ_s = 363.0 ± 14.6 ms; with a step to +70 mV, A_f = 0.39 ± 0.01, τ_f = 20.5 ± 1.2 ms, A_s = 0.63 ± 0.01, and τ_s = 388.7 ± 16.6 ms; after return to a protocol with no step to +70 mV, A_f = 0.40 ± 0.01, τ_f = 19.6 ± 1.4 ms, A_s = 0.6 ± 0.01, and τ_s = 354.9 ± 19.2 ms. **(D)** Average recovery time courses are shown for six cells for the indicated conditions. Initial control recovery after a 5-ms step to 0 mV: A_f = 0.51 ± 0.02, τ_f = 14.1 ± 1.0 ms, A_s = 0.51 ± 0.01, and τ_s = 328.1 ± 25.5 ms. Recovery following both the 5-ms inactivation step and the 50-ms step to +70 mV: A_f = 0.40 ± 0.01, τ_f = 22.3 ± 2.1 ms, A_s = 0.60 ± 0.01, and τ_s = 377.3 ± 25.8 ms. A repeat of recovery following just the 5-ms inactivation step to 0 mV: A_f = 0.44 ± 0.02, τ_f = 15.6 ± 1.3 ms, A_s = 0.56 ± 0.01, and τ_s = 337.9 ± 24.0 ms. **(E)** Mean and individual values for A_f, τ_f, and τ_s are shown for the set of six cells from D. There are small differences in A_f and τ_f observed with the +70 mV step, but similar to that which would expected from a 55-ms inactivation step to 0 mV (Fig. 4). All error bars in D and E are SD. Except as indicated in the middle panel, all *t*-test comparisons yielded P > 0.1. w/o, without.

between the start of each step (effective frequency of 66.6 Hz). Although this is a much higher frequency of stimulation than is ever observed in rodent CCs, this frequency provides a useful means of testing for use-dependent accumulation in slow recovery pathways. After a train of five brief depolarizations (Fig. 7 B), there is marked diminution in amplitude of the P2 response during recovery durations of 100 ms and less, with full recovery occurring by 3 s. With a train of 20 depolarizing steps (Fig. 7 C), there is only a small additional decrement in P2 currents at short recovery durations over that seen with a train of five steps. Recoveries from the cell shown in Fig. 7, A–D, are plotted in Fig. 7 E with compiled data (n = 19 cells) in Fig. 7 F. Overall, the fraction of recovery through fast pathways decreases from 0.5 ± 0.06 (mean ± SD; n = 19) following a single inactivation step to 0.27 ± 0.06 (same 19 cells) with a 20-pulse train (Fig. 7 G). In addition to the changes in amplitude ratios, the fast time constants exhibited some slowing as a function of number of pulses in a train (Fig. 7 H), while the slow time constants exhibited no change except for a small difference observed with the 20-pulse train (Fig.7 H). Overall, these results demonstrate that rat Nav currents exhibit a pronounced use dependence in Nav availability that arises from the differential recovery between the two separate inactivation pathways. It is important to realize that, whereas a five-pulse train of 5-ms steps (total of 25 ms depolarization) produces accumulation in slow recovering states, increasing a single 5-ms step to 25 ms has very little effect on the distribution between slow and fast recovering states (as in Fig. 4). Thus, during repetitive depolarizations, the separation between fast and slow pathways allows use-dependent accumulation of channels in slowly recovering states.

The protocol in Fig. 7 used a train frequency much higher than is ever observed in CCs. We therefore compared trains of ten 5-ms steps to 0 mV applied at frequencies of 1, 4, and 10 Hz. 1 Hz is the frequency at which some CCs spontaneously fire (Martinez-Espinosa et al., 2014; Vandael et al., 2015b), whereas small depolarizations can evoke firing with instantaneous frequencies up to 10–20 Hz (Solaro et al., 1995). Following inactivation produced by a single depolarization to 0 mV (Fig. 8 A), a 4-Hz train of 10 pulses (Fig. 8 B), or a 10-Hz train of 10 depolarizations (Fig. 8 C), variable recovery durations were applied to define the recovery time course. Qualitatively, increases in train frequency result in reductions in amplitude of currents evoked during P2, but these reductions are most apparent for recovery durations up through 100 ms (Fig. 8, B and C), whereas by 3 s, virtually all channels have recovered from inactivation. At all tested frequencies, peak Nav current evoked by sequential steps to 0 mV exhibits gradual reduction, with residual peak Nav current during a 66.7-Hz train being <0.1 of the initial peak current (Fig. 8 D). However, even at more physiologically appropriate frequencies (1, 4, and 10 Hz), the diminution of peak Nav amplitude indicates a slow accumulation of channels in inactivated states (Fig. 8 D). Furthermore, the time courses of recovery from inactivation (Fig. 8 E) show that the fraction of channels in fast recovery states is reduced as frequency is increased (Fig. 8 F). Increasing train frequency also appears to slow the fast component of recovery from inactivation, with little effect on the slow component of recovery (Fig. 8 G). Although the above results support the idea that there are two separable fast inactivation pathways with different rates of recovery, we note that the slowing of the fast recovery time constant with different train frequency (Fig. 8 F) is not obviously consistent with the simple model of two independent and competing inactivation and recovery mechanisms.

The results in Fig. 8 F indicate that, even at the nonphysiological stimulation frequency of 66.7 Hz, fractional accumulation in the slow recovery pathways is limited to ∼0.75. Might this reflect the possibility that some channels may not contain the fast inactivation/slow recovery machinery, or is it intrinsic to the kinetic properties of the two inactivation processes? We sought to address this issue by asking whether a simple approximation of the simple dual-pathway inactivation model could account quantitatively for the observations. To accomplish this, we used values for initial fractional availability before a train based on Fig. 1 E, and time constants of recovery from inactivation from Fig. 3 C. Furthermore, we assume that a 5-ms depolarization to 0 mV fully inactivates all available channels, with half of the channels entering slow recovery pathways and half into fast. Thus, all channels are assumed to exhibit the dual-pathway behavior. Based on this, we calculated the fractional occupancy of channels in closed states, slow recovery inactivated states, and fast recovery inactivated states for times immediately preceding each depolarization in the train, and then immediately after each depolarization in the train (schematized in Fig. S1 A). From the fraction of channels in closed states before each depolarization, the predicted run-down in peak Nav current was determined (Fig. S1, B and C) and matched very well with the measured decreases in Nav current with different train frequencies (Fig. 8 D). Calculations of state occupancy immediately preceding each depolarization in a train (Fig. S1 D) capture the expectations for use-dependent diminution of peak Nav amplitude. State occupancies calculated at the end of each 5-ms depolarization to 0 mV define the fractional occupancies that would be expected during a recovery protocol (Fig. S1, E and F). Plots of the fractional occupancy of channels in slow and fast recovery pathways (Fig. S1 D) show that at 1, 4, and 10 Hz, essentially all channels in fast recovery pathways recover during the 995-, 245-, and 95-ms recovery intervals. However, at 66.7 Hz, the 10-ms recovery interval is insufficient to allow full recovery from fast inactivation (Fig. S1 D, bottom). During a stimulus train, the slow decrease in fraction of channels in fast recovery pathways mirrors the slow increase in channels in slow recovery pathways. It is the occupancy in slow recovery states (Fig. S1 D) that determines the diminution of peak Nav current (Fig. S1 B).

Given that at 66.7-Hz stimulation, the peak Nav current can be reduced to <0.1 of initial peak value, why does the fraction of the slow component of recovery not exceed ∼0.75–0.8 (Fig. 8 F) in our recovery protocols? The state occupancies immediately after termination of each 5-ms depolarization better reflect what would be expected for the fraction of fast and slow recovery components during recovery from inactivation (Fig. S1, E and F). For the simplest case, we assumed that, irrespective of train frequency, recovery time constants were identical (Fig. S1 E). In

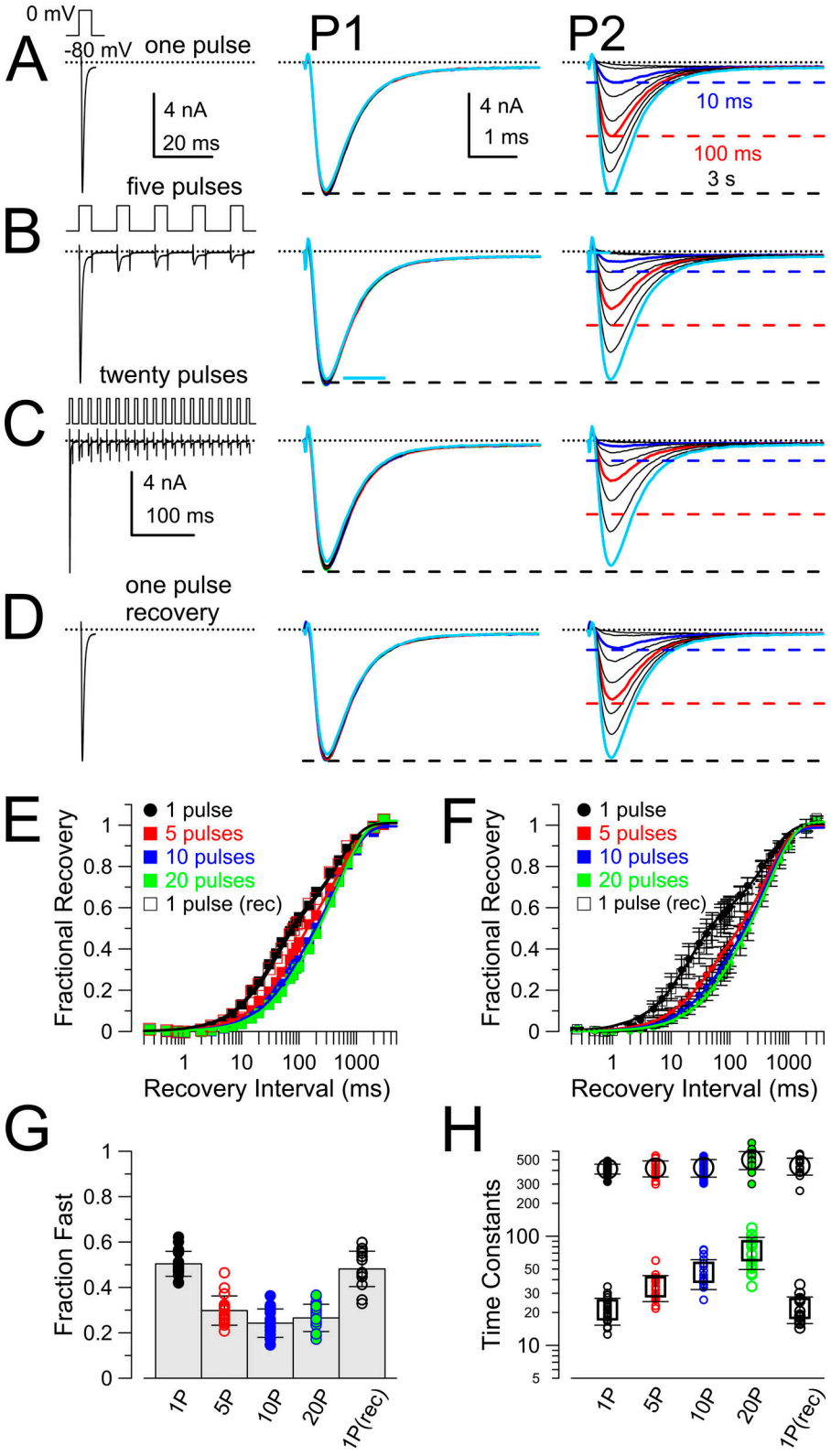

Figure 7. **Repetitive stimuli result in use-dependent accumulation of Nav channels in slow-recovering states. (A)** The standard paired pulse protocol was used to elicit Nav current with a 5-ms step to 0 mV (pulse 1, P1), with recovery intervals at −80 mV from 0.3 ms to 3 s preceding another 5-ms step (pulse 2, P2) to 0 mV. P1 currents are on the left, while P2 currents on the right followed recovery durations of 1, 3, 10, 20, 50, 100, 200, 500, and 3,000 ms. Horizontal colored lines and colored traces highlight traces following 10, 100, and 3,000 ms. **(B)** A train of five 5-ms steps to 0 mV was used as the P1 stimulus, with 10-ms intervals between steps to 0. Currents on the right are as in A. Traces at 10 (blue) and 100 (red) ms exhibit marked diminution compared with that in A. Dotted lines reflect the amplitudes of the recoveries for 10, 100, and 3,000 ms from A. **(C)** Traces are as in B, but for a train of twenty 5-ms steps to 0 mV, with 10 ms between each step in the train. Dotted lines on the right again correspond to fractional recoveries observed in A for 10, 100, and 3,000 ms. **(D)** Following stimulation with the trains, the standard single inactivation pulse was again applied, as in A, showing that, following a single inactivation step, fast recovery returns to its initial amplitude. **(E)** Fractional recovery from inactivation is plotted for the cell in A–D, with each curve fit with a two-exponential function with the following values: for initial control recovery, A_f = 0.49 ± 0.03, τ_f = 34.5 ± 3.0 ms, A_s = 0.52 ± 0.02, and τ_s = 481.3 ± 52.5; following the 5-pulse train, A_f = 0.40 ± 0.03, τ_f = 59.7 ± 6.0 ms, A_s = 0.60 ± 0.03, and τ_s = 515.6 ± 46.1 ms; following a 10-pulse train, A_f = 0.31 ± 0.05, τ_f = 68.4 ± 12.4 ms, A_s = 0.68 ± 0.05, and τ_s = 534.8 ± 58.3 ms; following a 20-pulse train, A_f = 0.29 ± 0.04, τ_f = 84.0 ± 12.5 ms, A_s = 0.73 ± 0.04, and τ_s = 562.8 ± 44.0 ms; after recovery, A_f = 0.47 ± 0.02, τ_f = 36.2 ± 3.2 ms, A_s = 0.54 ± 0.23, and τ_s = 475.3 ± 48.5 ms. **(F)** Averaged values (±SD) for fractional recovery are plotted for a set of 19 cells (recovery runs were only obtained for 16 of the cells). For the initial control protocol, recovery parameters (mean ± 90% confidence limit) are A_f = 0.50 ± 0.02, τ_f = 19.6 ± 1.4 ms, A_s = 0.51 ± 0.02, and τ_s = 404.3 ± 39.4 ms; for the 5-pulse P1 stimulus, A_f = 0.30 ± 0.02, τ_f = 33.6 ± 3.3 ms, A_s = 0.70 ± 0.02, and τ_s = 413.6 ± 22.9 ms; for the 10-pulse P1 stimulus, A_f = 0.24 ± 0.03, τ_f = 45.2 ± 6.4 ms, A_s = 0.75 ± 0.02, and τ_s = 418.6 ± 24.3 ms; for the 20-pulse P1 stimulus, A_f = 0.26 ± 0.04, τ_f = 67.6 ± 12.0 ms, A_s = 0.76 ± 0.04, and τ_s = 493.3 ± 38.0 ms; following return to the single pulse protocol, A_f = 0.48 ± 0.02, τ_f = 20.5 ± 1.7 ms, A_s = 0.53 ± 0.02, and τ_s = 436.3 ± 44.4 ms. **(G)** Mean values (±SD) of the fast recovery amplitude for each condition are plotted along with the best fit values from each individual cell in the set of 19 cells. Control (1P) and recovery (1P(rec)) fast amplitude differed from all other protocols (5P, 10P, 20P) at P = 0.000 (Kolmogorov–Smirnov test). 1P versus 1P(rec): 0.085; 5P versus 10P: 0.049; 5P versus 20P: 0.462; 10P versus 20P: 0.742. **(H)** Fast and slow time constants (±SD) are plotted for each of the recovery protocols, along with the individual determinations for each cell (small symbols). Kolmogorov–Smirnov P values for comparisons of fast time constant values were as follows: for 1P versus 5P, 0.000; 1P versus 10P, 0.000; 1P versus 20P, 0.000; 1P versus 1P(rec), 0.957; 5P versus 10P, 0.018; 5P versus 20P, 0.000; 10P versus 20P, 0.002; 20P versus. 1P(rec), 0.000. For comparisons of slow time constants: 1P differed from 5P, 10P, and 20P at 0.000; 1P versus 1P(rec), 0.354; 5P versus 10P, 0.116; 10P versus 20P, 0.956; 20P versus 1P(rec), 0.000.

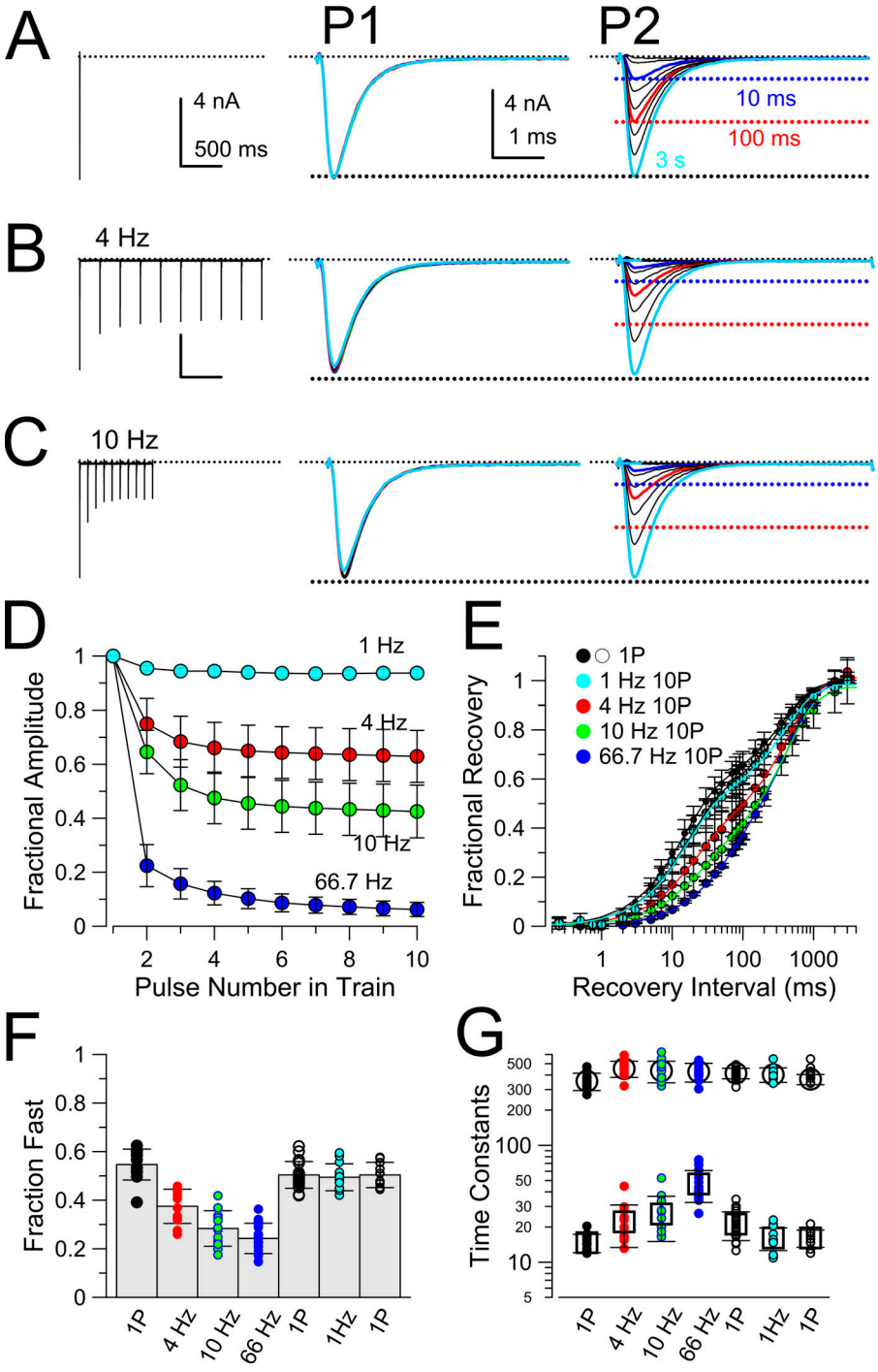

Figure 8. **Decrease in peak Nav amplitude during 10-pulse trains applied at different frequencies is associated with accumulation of channels in slow recovery pathways. (A)** A standard single 5-ms step to 0 mV was used to produce inactivation (pulse 1, P1), with recovery at −80 mV preceding a test step (pulse 2, P2) to 0 mV. Dotted lines highlight amplitude following 10, 100, and 3,000 ms of recovery. **(B)** From the same cell as in A, a 4-Hz, 10-pulse train of 5-ms steps to 0 mV was applied before the standard recovery step to −80 mV with dotted lines reflecting recovery amplitudes in A. **(C)** From the same cell as in A and B, a 10-Hz train preceded the recovery steps. **(D)** The decrement in peak Nav current amplitude is plotted for 1-, 4-, 10-, and 66.7-Hz trains of 10 pulses applied to 0 mV. Mean ± SD. **(E)** Time course of recovery from inactivation following different stimulus trains. 12 cells were used for 4- and 10-Hz trains, which also included a control set of recovery determinations with the standard single pulse (1P) protocol. 13 different cells were used for the 1-Hz protocol, which were also tested with the 1P protocol. 19 cells (same as in Fig. 7) were used with the 66.7-Hz 10P protocol, which also included the 1P protocol as a control. Fit values for 1P, 4-Hz, and 10-Hz cells were as follows. For 1P: A_f = 0.55 ± 0.02, τ_f = 14.7 ± 0.8 ms, A_s = 0.44 ± 0.02, and τ_s = 354.3 ± 17.2 ms; for 4 Hz, A_f = 0.37 ± 0.02, τ_f = 22.1 ± 2.5 ms, A_s = 0.64 ± 0.02, and τ_s = 453.2 ± 20.7 ms; and for 10 Hz, A_f = 0.28 ± 0.02, τ_f = 25.8 ± 3.1 ms, A_s = 0.69 ± 0.04, and τ_s = 433.7 ± 26.3 ms. For 1P and 1-Hz cells, 1P: A_f = 0.50 ± 0.02, τ_f = 16.1 ± 1.0 ms, A_s = 0.50 ± 0.02, and τ_s = 367.3 ± 13.0 ms; and for 1 Hz, A_f = 0.49 ± 0.02, τ_f = 16.1 ± 1.3 ms, A_s = 0.49 ± 0.02, and τ_s = 403.2 ± 20.3 ms. For 1P and 66.7-Hz cells, 1P: A_f = 0.50 ± 0.02, τ_f = 19.6 ± 1.9 ms, A_s = 0.51 ± 0.02, and τ_s = 404.3 ± 51.6 ms; and for 66.7 Hz, A_f = 0.24 ± 0.03, τ_f = 45.2 ± 8.6 ms, A_s = 0.75 ± 0.03, and τ_s = 493.3 ± 49.9 ms. **(F)** Means, standard errors, and individual values for the fitted fast component amplitude for all individual cells for the indicated stimulus protocols. Kolmogorov–Smirnov test P values for 12 cells compared with 1P, 4-Hz, and 10-Hz protocols: 1P versus 4 Hz, 0.000; 1P versus 10 Hz, 0.000; 4 Hz versus 10 Hz, 0.066. For 13 cells compared with 1P and 1 Hz protocols: 1P versus 1 Hz, 0.881. For 19 cells, compared with 1P and 66.7-Hz protocols: 1P versus 66.7 Hz, 0.000. **(G)** Mean ± SD and individual determinations of slow and fast time constants are displayed for the indicated conditions. For cells tested with 1P, 4 Hz, and 10 Hz protocols, Kolmogorov–Smirnov P values, for the fast recovery time constant, were 0.019 (1P versus 4 Hz), 0.001 (1P versus 10 Hz), and 0.433 (4 Hz versus 10 Hz). For the 1P versus 1 Hz train comparison, P = 0.638. For the 1P versus 66.7 Hz train comparison, P = 0.000. For slow time constants, for 1P versus 4 Hz, P = 0.001; for 1P versus 10 Hz, P = 0.186; for 4 Hz versus 10 Hz, P = 0.186. For the 1P versus 1 Hz train comparison, P = 0.341. for the 1P versus 66.7 Hz comparison, P = 0.462.

this case, as train frequency increases, the fraction of channels in fast recovery pathways monotonically decreases (Fig. S1 G), with a value of ∼0.1 after 10 pulses. This deviates from the experimentally observed tendency of the fast component to reach a limit of ∼0.2–0.25 fractional availability. However, our measurements also revealed that the apparent fast time constant after a 10-pulse train is slowed at higher train frequencies (Fig. 8 F). We therefore modeled expectations for fast and slow components with the assumption that the fast time constant slows with train frequency (Fig. S1 F). Although a slower fast time constant of recovery has little impact on the fractions of slow and fast components at 1, 4, and 10 Hz (Fig. S1 F, top three panels), the value of the fast time constant substantially impacts the overall rate of accumulation in slow recovery pathways for 66.7 Hz

stimulation (Fig. S1 F, bottom), and also impacts the fractional occupancies in slow and fast pathways after long trains (Fig. S1, F and G). Thus, based on experimentally measured values, the dual-pathway behavior generally recapitulates the frequency-dependence reductions in Nav current amplitude and also the general properties of the frequency dependence of changes in the fraction of fast recovery channels (Fig. S1 G). This analysis suggests that, even if all channels exhibit the dual-pathway inactivation behavior, high-frequency stimulation may not necessarily drive all channels into slow recovery pathways with the protocols we have employed.

Nav current availability is markedly reduced by repetitive AP clamp waveforms

In the above analysis, we have focused on protocols that define properties of the dual-pathway fast inactivation following depolarizations that produce full activation and during conditions in which recovery to resting states predominates. However, the normal resting potential of CCs, typically considered between −45 and −55 mV (Martinez-Espinosa et al., 2014; Vandael et al., 2015b), spans a range in which there is likely to be considerable equilibration of channels in and out of closed, inactivated, and, to some extent, open states. Here, to assess the impact of holding potential and firing frequency on Nav availability under conditions more reflective of physiological circumstances, we have used AP-like waveforms to examine changes in Nav availability during repetitive activity. To accomplish this, a spontaneously occurring AP was recorded from a rat CC and then used as a voltage-clamp command. The AP waveform included 5 ms at −52 mV before the upswing of the AP and then a period of ∼35 ms corresponding to an afterhyperpolarization. Experiments were done on dissociated CCs maintained in short-term culture, which allowed the use of perforated-patch recording methods, with 20 mM cytosolic Cs^+ to inhibit outward current. AP clamp waveforms were applied at frequencies of 4, 10, or 20 Hz at holding potentials between the AP waveform. With 120 mM extracellular Na^+ and 2 mM extracellular Ca^{2+}, the currents evoked by the AP clamp waveform exhibit a biphasic inward current (Fig. 9 A), with strong inward current activated during the rising phase of the AP command waveform, essentially 0 net inward current at the AP peak, and then a secondary reduced peak of inward current during AP repolarization. The amplitude of the initial inward current during the AP rising phase exhibits strong suppression at a 10 Hz AP frequency, while the amplitude of the secondary inward current is unaltered at 10 Hz. This indicates that essentially all Nav current is fully inactivated at the time of the secondary phase of inward current during the first AP in a train and that the secondary inward current likely arises exclusively from voltage-dependent Ca^{2+} (Cav) current. Using this approach, the impact of different holding potentials (−50, −60, −70, and −80 mV) both before and between the AP waveforms was examined (Fig. 9 B). As expected from the steady-state inactivation behavior of the Nav current, the maximum peak inward current activated by the AP clamp waveform varied substantially over holding potentials from −50 mV through −80 mV. Furthermore, as shown for AP waveforms applied at 10 Hz, at all recovery potentials there was marked diminution of the AP waveform–evoked Nav current (Fig. 9 B).

When the AP-evoked peak inward current amplitudes are plotted as a function of the overall elapsed time of the train of AP commands (Fig. 10, A–C), the initial peak inward current is reduced as holding potential is made more positive. Irrespective of train frequency, a gradual reduction in Nav current amplitude occurs over the first 5–6 APs, largely reaching a plateau after that (Fig. 10, A–C). At −50 mV holding potential, the peak inward current can be reduced at a 10-Hz AP frequency to <20% of that available from a −80-mV holding potential (Fig. 10 B). Even at a 4-Hz frequency, the peak Nav current amplitude from a holding potential of −50 mV is reduced to ∼20% of the peak that would have been from a −80 mV holding potential (Fig. 10 A). Overall, this experiment indicates that, during normal AP frequencies and at reasonable membrane potentials, Na^+ channel availability is quickly reduced to ∼10–25% of the full availability, with essentially all Nav channels being inactivated during a single AP waveform.

To evaluate whether these decrements in AP-evoked currents might be consistent with the measured properties of dual-pathway inactivation, we followed the general procedures outlined for Fig. S1, taking into account the specific details of the AP train waveforms (Fig. 9 B). Using measured time constants of recovery from inactivation at different voltages (Fig. 3 C), the calculated decrements in evoked current amplitude during a train of 10 AP clamp waveforms (Fig. 10, D–F) closely follow the measured decreases (Fig. 10, A–C). Furthermore, we also computationally tested removal of slow recovery from inactivation, with the assumption that all inactivation is by a single fast inactivation pathway (dotted lines in Fig. 10, D–F). With 10-Hz and 20-Hz trains, an initial decrement in peak Nav current amplitude is predicted, but this is complete within 2–3 APs, consistent with the absence of any slow accumulation of channels in slow-recovering inactivated states. We also recast the results and analysis in Fig. 10, A–F, to better focus on comparisons among different train frequencies at a single holding potential. The correspondence of the measured changes in Nav current amplitude (Fig. 10, G–I) with the calculated changes (Fig. 10, J–L) based on the two separable inactivation pathways idea provides further support for this idea and illustrates the importance of the slow recovery pathways in defining changes in Nav availability during AP trains in CCs. When the fractional occupancies of channels in available, slow recovery inactivated, and fast recovery inactivated states are determined (Fig. S2), the analysis shows clearly that occupancy of channels in slow recovery states is the major determinant of the reduction in AP-evoked Nav current amplitude.

Discussion

The present results establish that rapid inactivation of Nav current in rat CCs involves entry into two distinct pathways of fast inactivation, each with distinct rates of recovery from inactivation. Here, we first contrast the slow recovery process described here with traditional slow Nav inactivation. We then consider potential implications of this dual-pathway

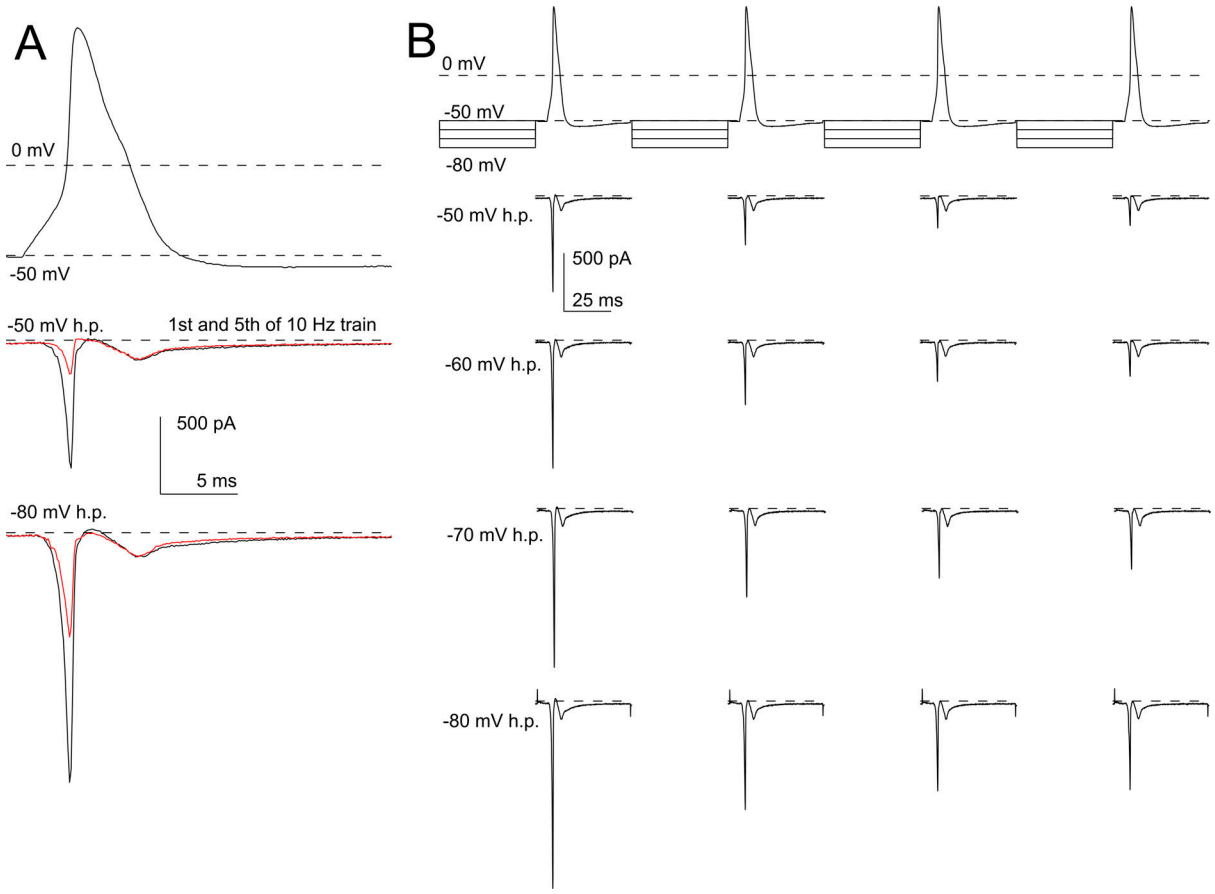

Figure 9. **Inactivation of Nav current by AP clamp waveforms. (A)** Top trace shows an AP recorded from a rat CC with the perforated patch-method with normal Na^+ and K^+ gradients. The AP waveform was then used as a voltage-clamp waveform for all traces in A and B. For a given train of AP clamp waveforms, a cell was held at different holding potentials, −50 through −80 mV, before and between each AP clamp waveform. For the example in A, 100 ms separated the initiation of each individual AP clamp waveform. The traces below the AP waveform show currents activated from a holding potential (h.p.) of −50 mV or −80 mV (bottom), for the first and fifth evoked current in a 10 Hz train. Note that the inward current during the falling phase of the AP command waveform does not change in amplitude between the first and fifth waveform, reflecting Cav current, while the early inward current shows marked diminution, indicative of Nav current inactivation. **(B)** The full command waveforms for the first four APs in a 10-pulse train are shown along with the currents evoked by the AP command waveforms for holding potentials from −50 mV through −80 mV.

inactivation for AP firing in CCs. Although the variety of protocols used here to probe the contributions of the two pathways might seem suitable for evaluation of gating models, until the molecular determinants and potential interactions between the pathways are directly tested, we feel any attempt to model extensively the present observations is premature.

Slow recovery of Nav channels from inactivation

Slow components of recovery from inactivation have been observed in a number of preparations, including squid giant axons (Chandler and Meves, 1970; Rudy, 1978), *Myxicola infundibulum* axons (Rudy, 1981), and rat sympathetic neurons (Belluzzi and Sacchi, 1986). Typically, such slow recovery from inactivation is a process that also develops slowly, with increases in the duration of the inactivation step leading to increases in the fraction of current that recovers slowly (Silva, 2014). Such slow inactivation behavior, which is thought to involve coupling of slow inactivation to fast inactivation, modeled as in Scheme 1, has been proposed to apply to the cardiac Nav channel, Nav1.5 (Zhang et al., 2013), and other cases (Silva, 2014). Essentially, because slow inactivation is preceded by entry into fast inactivated states, the sojourn of time in fast inactivated states results in accumulation in slow inactivated states.

In contrast to conventional slow inactivation just described, here the results argue strongly for two functionally distinct competing fast inactivation pathways, with one pathway having slower recovery kinetics. Perhaps the first proposal for the idea of two competing inactivation pathways with different recovery kinetics was that for inactivation of Nav current in *M. infundibulum* axons (Rudy, 1981). However, in that case, the slow recovery was much slower than observed here and appears unlikely to play much role under physiological conditions. More recently, as new information regarding the properties of various mammalian Nav channel variants has appeared, additional examples of Nav currents with slow recovery properties likely to be of physiological importance have appeared (Lou et al., 2005; Goldfarb et al., 2007; Shakkottai et al., 2009; Milescu et al., 2010; Venkatesan et al., 2014; Navarro et al., 2020). One of the most intriguing examples, perhaps relevant to our findings with rat CC Nav current, concerns slow recovery from inactivation of

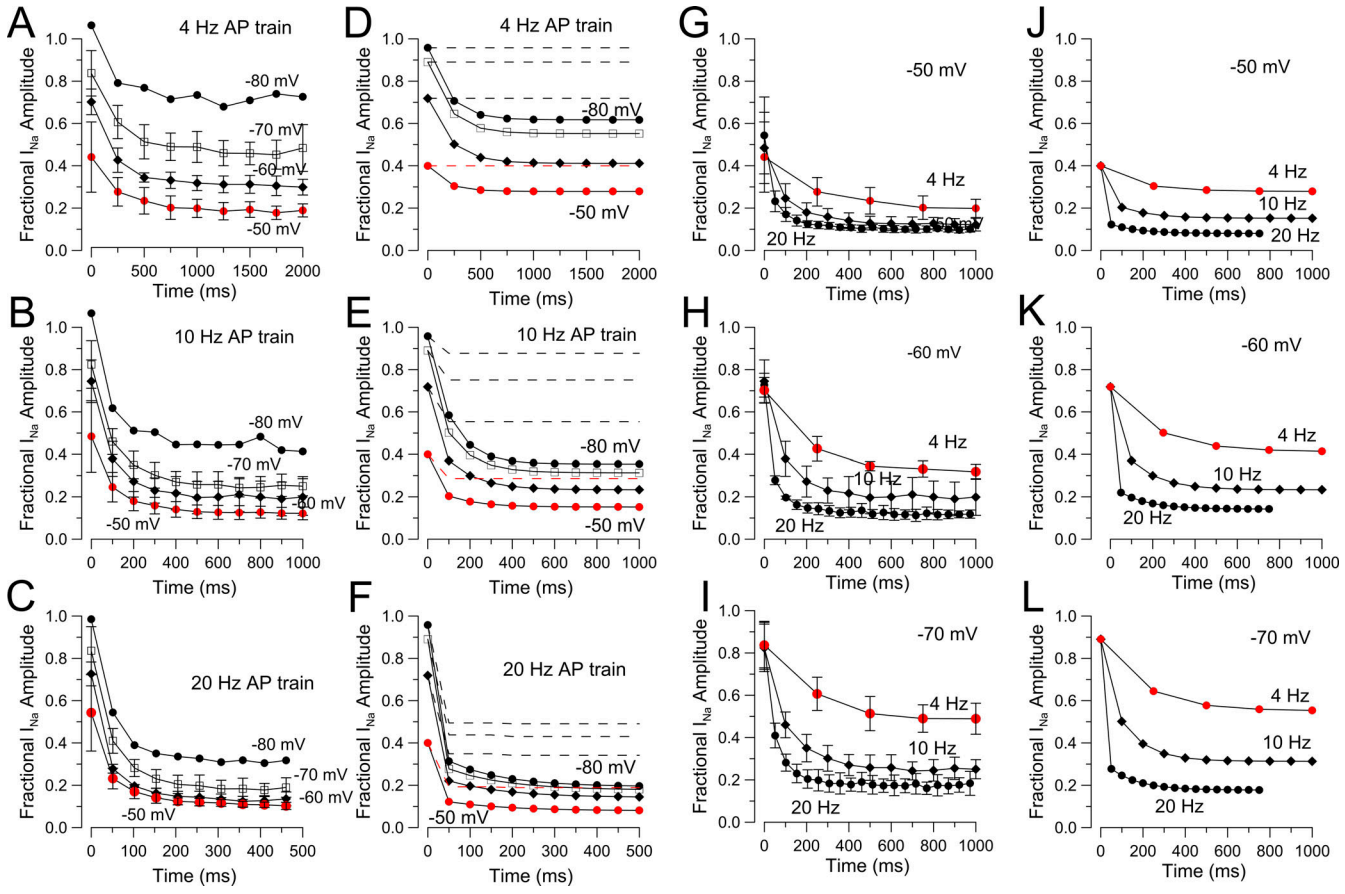

Figure 10. **Diminution of AP-evoked peak inward current with different holding potentials and AP frequencies. (A)** Peak inward current evoked by each AP clamp waveform applied at 4 Hz was normalized to the maximal available current defined in a given cell using a standard Nav activation protocol (Fig. 1 A) from a holding potential of −80 mV. At −50 mV, the initial AP is reduced in amplitude by ∼50% compared with that from −80 mV and diminishes to <20% by the fifth AP command. The time base corresponds to the total elapsed time of the protocol as shown in Fig. 1 B. Number of cells: −50 mV, *n* = 4; −60 mV, *n* = 3; −70 mV, *n* = 2; −80 mV, *n* = 1. Error bars here and in other panels are SD. **(B)** Normalized inward current amplitude at different resting/holding potentials is shown for a 10-Hz AP train. **(C)** Normalized inward current amplitude is shown for a 20-Hz AP train. **(D)** Predicted decrements in peak Nav current were calculated as follows. Availability at a given holding potential was determined from the steady-state inactivation curve (Fig. 1 E) with a 250-ms prepulse. Measured fast and slow recovery time constants (Fig. 3 C) were used to calculate fractional recovery during given sojourns at particular voltages. The predicted decrement based on the protocol of Fig. 10 B was calculated for the 4-Hz AP train, assuming that all Nav current inactivates during each AP, with the first AP driving half the channels into a slow recovery pathway and half into a fast recovery pathway. Recovery than occurs following the AP for a period of 36 ms corresponding to an afterhyperpolarization ranging from −56 to −50 mV; for simplicity, we assumed −50 mV for this interval. Then, the additional recovery that occurs during the interval between sweeps at the specified recovery voltages of −50, −60, −70, or −80 mV was calculated. For comparison, the calculated AP decrement when all inactivation is exclusively via a fast recovery pathway is also shown (dotted lines; red dotted line indicates −50 mV). **(E)** The same calculations as in D were done for a 10-Hz train showing the deeper decrement in AP amplitudes, because of slower recovery intervals. **(F)** Fractional decrement in AP amplitude calculated for the 20-Hz train is shown. **(G)** The data from A–C are recast to directly compare 4-, 10-, and 20-Hz trains all for a given holding potential (−50 mV). **(H)** As in G, but for −60 mV. **(I)** As in G, but for −70 mV. **(J–L)** The calculated decrements for the conditions plotted in G–I are shown.

Nav1.6 current observed in cerebellar granule cells (Goldfarb et al., 2007; Dover et al., 2010; Goldfarb, 2012). In this case, a slow component of recovery from inactivation has been attributed to members of a family of cytosolic proteins called iFGFs (but also termed FHFs; Olsen et al., 2003; Wittmack et al., 2004). The inactivation behavior of Nav1.6 current, either when coexpressed with particular iFGFs or as the native cerebellar granule cell Nav current, is well described by a dual-pathway, fast inactivation model similar to that given in Scheme 2, as first proposed by Goldfarb et al. (2007). Inactivation mediated by certain iFGFs is proposed to compete with the intrinsic fast inactivation particle. As a consequence of the slower recovery from inactivation arising from iFGF-mediated inactivation, accumulation of channels in more slowly recovering states can occur. A similar model has also been used to describe Nav current behavior in dorsal raphe neurons (Milescu et al., 2010). The latter case may be more applicable to the present situation in rat CCs, since the dorsal rat raphe neurons typically fire at frequencies only up to 5–20 Hz, while the cerebellar granule cells fire at frequencies in excess of 50 Hz. Two important points regarding this dual-pathway inactivation process are, first, that rates of entry into both the fast and slow recovering populations are comparable, and second, that there is no equilibration between the two pathways, i.e., they are strictly competitive inactivation processes (Goldfarb, 2012). In the case of iFGF-mediated inactivation, it has been proposed that the N termini

of A-isoforms of iFGFs can move into a position of occlusion in specific Nav channels (Dover et al., 2010; Goldfarb, 2012; Venkatesan et al., 2014), competing with the ability of the IFM (isoleucine/phenylalanine/methionine) triplet of residues in the DIII/DIV α-helical loop of an Nav α subunit to mediate conventional fast inactivation (Patton et al., 1992; West et al., 1992; O'Leary et al., 1995). Both inactivation mechanisms share a simple 1:1 stoichiometry with each Nav α subunit. A Nav channel contains a single IFM triplet in the DIII/DIV loop that participates in conventional fast inactivation, while iFGFs bind to a single interface on the Nav cytosolic C-terminal domain (Goetz et al., 2009; Wang et al., 2012). Mutations of specific FGF residues that influence binding at this interface underlie some naturally occurring diseases of excitability (Laezza et al., 2007; Hennessey et al., 2013).

Although the present results do not provide any information about the molecular underpinnings of the slower recovery component of fast inactivation in rat CCs, our experiments do place some limits on the relationship between the two inactivation pathways. First, once inactivation has occurred at potentials of 0 mV and more positive, channels that have entered states leading to fast recovery do not seem to interconvert with channels in slow recovery pathways over times of 4–100 ms. Although we observed some diminution in the relative fraction of the fast component with inactivation pulse duration, the time course of this gradual diminution may be better explained by the slow onset of traditional slow inactivation. Second, the relative fraction of channels entering either slower or faster recovery pathways is largely voltage-independent at voltages >0 mV. Third, once channels have inactivated, stronger additional depolarizations only weakly influence the distribution of channels among states leading to slow and fast recovery paths. These results are all consistent with the idea that two rapidly entered inactivating pathways exhibit essentially no equilibration between them once inactivation has occurred. Overall, these behaviors are consistent with the general inactivation model outlined in Scheme 2, with the uncertainty that our results provide no information about the extent to which entry into I_{SR} states may occur from closed Nav channels. Goldfarb (2012) has proposed that the iFGF-dependent inactivation can occur from at least up to two or three of the closed states preceding opening, whereas the I_{SR} component of Nav current in dorsal raphe neurons was modeled with inactivation only occurring from open Nav channels (Milescu et al., 2010). The extent to which closed-state inactivation may occur from each of the two competing fast inactivation processes may impact importantly on use-dependent changes in channel availability, and this will be an important topic for future work. In sum, the results presented here have highlighted several key properties of slow recovery from inactivation of Nav current in CCs that distinguishes it from the traditional slow inactivation (Zhang et al., 2013; Silva, 2014).

Potential physiological consequences of dual-pathway, fast inactivation in electrical activity of rodent CCs

Rodent CCs express a diverse set of ionic conductances (Lingle et al., 2018; Carbone et al., 2019), which together are critical in defining the temporal properties of Ca^{2+} elevations, essential to evoke secretion of catecholamines (Borges et al., 2018). This includes Cav1.2 and Cav1.3 subtypes of Ca^{2+} channels (Mahapatra et al., 2012), small conductance Ca^{2+}-activated K^+ channels (Vandael et al., 2012), BK-type Ca and voltage-activated K^+ channels (Solaro et al., 1995), and voltage-gated potassium channels, in addition to Nav channels. Although CA secretion in rodent CCs is not tightly linked to Ca^{2+} influx arising from single APs, brief trains of AP activity promote secretion driven by increases in cytosolic Ca (Duan et al., 2003). Given the constellation of conductances found in CCs, CCs can exhibit a variety of types of electrical activity spanning quiescence, rhythmic spontaneous APs driven largely by Cav channels (Vandael et al., 2015a), and slow-wave bursts influenced by both BK channel properties (Martinez-Espinosa et al., 2014) and Nav availability (Vandael et al., 2015b). However, maximal firing rates never exceed ∼15–20 Hz (Solaro et al., 1995; Martinez-Espinosa et al., 2014; Carbone et al., 2019). In addition to the intrinsic conductances, electrical activity in CCs can be influenced either directly via depolarization arising from ligand-gated channel activation by splanchnic nerve released factors such as acetylcholine or via G-protein–coupled receptor activation resulting in Ca^{2+} elevations or modulation of ion channels (Carbone et al., 2019).

How might the unique properties of Nav inactivation described here relate to previous results pertinent to the role of Nav channels in CC excitability? Two features of Nav channels during CC electrical activity may reflect the important role of slow recovery from inactivation. First, square wave depolarization of either rat (Solaro et al., 1995) or mouse (Martinez-Espinosa et al., 2014) CCs drives AP firing that exhibits significant attenuation in both interspike interval and AP amplitude. However, CCs with BK channels containing inactivating BK currents arising from the presence of the β2 regulatory subunit better support sustained AP firing than cells lacking β2 subunits (Martinez-Espinosa et al., 2014). Because β2 subunits shift BK gating to more negative voltages, thereby allowing more robust afterhyperpolarizations, it has been suggested that the β2-containing BK channels may promote recovery of Nav channels from inactivation, thereby sustaining repetitive firing (Solaro et al., 1995; Lingle et al., 1996). Although recovery from conventional fast inactivation would also be enhanced by the presence of β2-containing BK channels, if CC Nav channels only manifested a conventional fast inactivation mechanism, it would be expected that CCs should readily sustain firing at 20 Hz without any diminution in AP amplitude. Therefore, we would suggest that, in addition to the well-established role of cumulative activation of SK channels in produced AP amplitude attenuation and spike frequency adaptation (Vandael et al., 2012), accumulation of Nav channels in inactivated states that exhibit slow recovery may also play a similar role (Fig. 10). In addition, accumulation of Nav channels in slow recovery pathways may also underlie the observed role of Nav availability in defining the transition of CCs from spontaneously firing cells to slow-wave bursting cells (Vandael et al., 2015a; Guarina et al., 2017). Specifically, modest depolarization of CCs elicited by lowering extracellular pH and producing mild Nav inactivation favors transition of CC firing from spontaneous firing to slow-wave

bursts dominated by Ca^{2+} APs. With appropriate models of CC Nav gating behavior, in the future it should prove possible in dynamic clamp experiments to explicitly evaluate the impact of conventional fast inactivation versus dual-pathway fast inactivation on patterns of CC electrical activity.

Comparing dual-pathway fast inactivation in CCs to recovery from inactivation in other cells

Qualitatively similar dual-pathway fast inactivation has been described in cerebellar granule cells (Goldfarb et al., 2007), hippocampal pyramidal neurons (Venkatesan et al., 2014), and raphe neurons (Milescu et al., 2010; Navarro et al., 2020). In all cases, accumulation of Nav channels in slow recovery pathways influences Nav availability and firing frequency, although the granule cell and pyramidal cell measurements do not allow quantitative assessments of the relative entry into fast and slow recovery paths from single APs. In contrast, the work on raphe neurons allows more facile comparison to the phenomenology described here. Whereas for CCs, a single 5-ms depolarization drives channels into about half fast recovery and half slow recovery pathways, in the raphe neurons, only 20% of activated channels enter slow recovery pathways and 80% fast recovery pathways (Milescu et al., 2010; Navarro et al., 2020). Experimentally, 20-Hz trains can drive raphe Nav channels into ∼50% slow recovery and theoretically higher (Navarro et al., 2020), whereas in CCs, Nav channels appear to be limited to ∼75% occupancy in the slow recovery pathways. Although such differences might be discounted as simply being the likely consequence of different molecular underpinnings, the differences may be physiologically instructive and point to important future topics for investigation. The distribution of channels between slow and fast recovery pathways following an AP or brief depolarization might be influenced by two primary factors. One possibility is that there may be differences in the relative expression of a regulatory subunit that contributes to the slow recovery process, such that on average, not all Nav channels in a cell may contain the necessary regulatory subunit. For both the raphe cells and the CCs, we think this is unlikely. In the raphe cells, modeling is consistent with the idea that channels can be driven almost completely into slow recovery pathways. For the CCs, although we were unable to drive channels into more than ∼75% slow recovery, examination of the impact of fast and slow recovery rates on the state occupancies suggests that the kinetics of the recovery processes relative to the recovery intervals in the higher-frequency trains can limit slow recovery pathway occupancy. A second possibility is that, although both fast inactivation pathways are entered during brief depolarization, in different types of cells, the relative rate of onset of the two types of fast inactivation processes may differ. For CCs, we have no direct measurements of the rates of entry into traditional fast inactivation, but that we observed 50% fast inactivated and 50% slow inactivated suggests the rates are comparable. For the raphe neurons, it is possible that the rate of normal fast inactivation is simply fourfold faster than the inactivation leading to slow recovery. One difference in the kinetic properties of the dual-pathway processes between CCs and raphe neurons is that the fast and slow recovery time constants differ by ∼20-fold in CCs (Fig. 3 C), whereas in raphe neurons, they differ by ∼100-fold (Milescu et al., 2010). Such a difference, whatever its molecular basis, could play a critical role in defining the dynamic range of Nav availability and firing properties in a given neuron.

Possible molecular underpinnings of dual-pathway fast inactivation in CCs

The identity of the specific Nav subtype that underlies Nav currents in rat CCs remains unresolved. Although long-term dogma has suggested that CC Nav current is primarily Nav1.7 (Wada et al., 2008; Tamura et al., 2014), knockout of Nav1.3 removes Nav current in most mouse CCs (Martinez-Espinosa et al., 2021), leaving only a smaller contribution in some cells of some other Nav current, perhaps Nav1.7. We would suggest the rat CCs may contain both Nav1.3 and Nav1.7, with perhaps a larger component of Nav1.7 than found in mouse CCs (Martinez-Espinosa et al., 2021). Regarding the basis for the slow component of recovery, all tests of the rat CC Nav current properties here point to the idea that the rat CC Nav current exhibits two independent fast inactivation processes. Presumably, one corresponds to conventional fast Nav inactivation, while the other remains undefined. In the associated paper, iFGF14 is shown to critically determine slow recovery from inactivation in mouse CCs (Martinez-Espinosa et al., 2021). We anticipate that the results presented here will serve as a foundation for quantitative evaluation of the dual-pathway inactivation behavior and how it may impact on excitability, once the molecular determinants of that process are clearly defined.

Acknowledgments

Olaf S. Andersen served as editor.

We thank M. Prakriya for valuable contributions during the early stages of this work.

This work was supported by the National Institute of Neurological Disorders and Stroke (grant NS100695).

The authors declare no competing financial interests.

Author contributions: P.L. Martinez-Espinosa, A. Neely, and J. Ding contributed to whole-cell recording experiments and designed and analyzed data. J. Ding was responsible for current-clamp experiments. C.J. Lingle contributed to the design, analysis, and interpretation of the results and wrote the paper. All authors have approved the final version of the paper.

Submitted: 1 October 2020
Revised: 7 January 2021
Accepted: 19 January 2021

References

Barbosa, C., and T.R. Cummins. 2016. Unusual Voltage-Gated Sodium Currents as Targets for Pain. *Curr. Top. Membr.* 78:599–638. https://doi.org/10.1016/bs.ctm.2015.12.005

Belluzzi, O., and O. Sacchi. 1986. A quantitative description of the sodium current in the rat sympathetic neurone. *J. Physiol.* 380:275–291. https://doi.org/10.1113/jphysiol.1986.sp016285

Borges, R., L. Gandía, and E. Carbone. 2018. Old and emerging concepts on adrenal chromaffin cell stimulus-secretion coupling. *Pflugers Arch.* 470:1–6. https://doi.org/10.1007/s00424-017-2082-z

Bosch, M.K., Y. Carrasquillo, J.L. Ransdell, A. Kanakamedala, D.M. Ornitz, and J.M. Nerbonne. 2015. Intracellular FGF14 (iFGF14) Is Required for Spontaneous and Evoked Firing in Cerebellar Purkinje Neurons and for Motor Coordination and Balance. *J. Neurosci.* 35:6752–6769. https://doi.org/10.1523/JNEUROSCI.2663-14.2015

Brickley, S.G., M.I. Aller, C. Sandu, E.L. Veale, F.G. Alder, H. Sambi, A. Mathie, and W. Wisden. 2007. TASK-3 two-pore domain potassium channels enable sustained high-frequency firing in cerebellar granule neurons. *J. Neurosci.* 27:9329–9340. https://doi.org/10.1523/JNEUROSCI.1427-07.2007

Capes, D.L., M.P. Goldschen-Ohm, M. Arcisio-Miranda, F. Bezanilla, and B. Chanda. 2013. Domain IV voltage-sensor movement is both sufficient and rate limiting for fast inactivation in sodium channels. *J. Gen. Physiol.* 142:101–112. https://doi.org/10.1085/jgp.201310998

Carbone, E., R. Borges, L.E. Eiden, A.G. García, and A. Hernández-Cruz. 2019. Chromaffin Cells of the Adrenal Medulla: Physiology, Pharmacology, and Disease. *Compr. Physiol.* 9:1443–1502. https://doi.org/10.1002/cphy.c190003

Carter, B.C., and B.P. Bean. 2011. Incomplete inactivation and rapid recovery of voltage-dependent sodium channels during high-frequency firing in cerebellar Purkinje neurons. *J. Neurophysiol.* 105:860–871. https://doi.org/10.1152/jn.01056.2010

Chandler, W.K., and H. Meves. 1970. Slow changes in membrane permeability and long-lasting action potentials in axons perfused with fluoride solutions. *J. Physiol.* 211:707–728. https://doi.org/10.1113/jphysiol.1970.sp009300

Chiu, S.Y. 1977. Inactivation of sodium channels: second order kinetics in myelinated nerve. *J. Physiol.* 273:573–596. https://doi.org/10.1113/jphysiol.1977.sp012111

Choi, J.S., S.D. Dib-Hajj, and S.G. Waxman. 2007. Differential slow inactivation and use-dependent inhibition of Nav1.8 channels contribute to distinct firing properties in IB4+ and IB4- DRG neurons. *J. Neurophysiol.* 97:1258–1265. https://doi.org/10.1152/jn.01033.2006

Cummins, T.R., J.R. Howe, and S.G. Waxman. 1998. Slow closed-state inactivation: a novel mechanism underlying ramp currents in cells expressing the hNE/PN1 sodium channel. *J. Neurosci.* 18:9607–9619. https://doi.org/10.1523/JNEUROSCI.18-23-09607.1998

Cummins, T.R., F. Aglieco, M. Renganathan, R.I. Herzog, S.D. Dib-Hajj, and S.G. Waxman. 2001. Nav1.3 sodium channels: rapid repriming and slow closed-state inactivation display quantitative differences after expression in a mammalian cell line and in spinal sensory neurons. *J. Neurosci.* 21:5952–5961. https://doi.org/10.1523/JNEUROSCI.21-16-05952.2001

Dib-Hajj, S.D., L. Tyrrell, T.R. Cummins, J.A. Black, P.M. Wood, and S.G. Waxman. 1999. Two tetrodotoxin-resistant sodium channels in human dorsal root ganglion neurons. *FEBS Lett.* 462:117–120. https://doi.org/10.1016/S0014-5793(99)01519-7

Dover, K., S. Solinas, E. D'Angelo, and M. Goldfarb. 2010. Long-term inactivation particle for voltage-gated sodium channels. *J. Physiol.* 588:3695–3711. https://doi.org/10.1113/jphysiol.2010.192559

Duan, K., X. Yu, C. Zhang, and Z. Zhou. 2003. Control of secretion by temporal patterns of action potentials in adrenal chromaffin cells. *J. Neurosci.* 23:11235–11243. https://doi.org/10.1523/JNEUROSCI.23-35-11235.2003

Fenwick, E.M., A. Marty, and E. Neher. 1982. Sodium and calcium channels in bovine chromaffin cells. *J. Physiol.* 331:599–635. https://doi.org/10.1113/jphysiol.1982.sp014394

Goetz, R., K. Dover, F. Laezza, N. Shtraizent, X. Huang, D. Tchetchik, A.V. Eliseenkova, C.F. Xu, T.A. Neubert, D.M. Ornitz, et al. 2009. Crystal structure of a fibroblast growth factor homologous factor (FHF) defines a conserved surface on FHFs for binding and modulation of voltage-gated sodium channels. *J. Biol. Chem.* 284:17883–17896. https://doi.org/10.1074/jbc.M109.001842

Goldfarb, M. 2005. Fibroblast growth factor homologous factors: evolution, structure, and function. *Cytokine Growth Factor Rev.* 16:215–220. https://doi.org/10.1016/j.cytogfr.2005.02.002

Goldfarb, M. 2012. Voltage-gated sodium channel-associated proteins and alternative mechanisms of inactivation and block. *Cell. Mol. Life Sci.* 69:1067–1076. https://doi.org/10.1007/s00018-011-0832-1

Goldfarb, M., J. Schoorlemmer, A. Williams, S. Diwakar, Q. Wang, X. Huang, J. Giza, D. Tchetchik, K. Kelley, A. Vega, et al. 2007. Fibroblast growth factor homologous factors control neuronal excitability through modulation of voltage-gated sodium channels. *Neuron.* 55:449–463. https://doi.org/10.1016/j.neuron.2007.07.006

Guarina, L., D.H. Vandael, V. Carabelli, and E. Carbone. 2017. Low pH_o boosts burst firing and catecholamine release by blocking TASK-1 and BK channels while preserving Cav1 channels in mouse chromaffin cells. *J. Physiol.* 595:2587–2609. https://doi.org/10.1113/JP273735

Hains, B.C., J.P. Klein, C.Y. Saab, M.J. Craner, J.A. Black, and S.G. Waxman. 2003. Upregulation of sodium channel Nav1.3 and functional involvement in neuronal hyperexcitability associated with central neuropathic pain after spinal cord injury. *J. Neurosci.* 23:8881–8892. https://doi.org/10.1523/JNEUROSCI.23-26-08881.2003

Hennessey, J.A., C.A. Marcou, C. Wang, E.Q. Wei, C. Wang, D.J. Tester, M. Torchio, F. Dagradi, L. Crotti, P.J. Schwartz, et al. 2013. FGF12 is a candidate Brugada syndrome locus. *Heart Rhythm.* 10:1886–1894. https://doi.org/10.1016/j.hrthm.2013.09.064

Herrington, J., C.R. Solaro, A. Neely, and C.J. Lingle. 1995. The suppression of $Ca^{(2+)}$- and voltage-dependent outward K^+ current during mAChR activation in rat adrenal chromaffin cells. *J. Physiol.* 485:297–318. https://doi.org/10.1113/jphysiol.1995.sp020731

Herzog, R.I., T.R. Cummins, F. Ghassemi, S.D. Dib-Hajj, and S.G. Waxman. 2003. Distinct repriming and closed-state inactivation kinetics of Nav1.6 and Nav1.7 sodium channels in mouse spinal sensory neurons. *J. Physiol.* 551:741–750. https://doi.org/10.1113/jphysiol.2003.047357

Hille, B. 2001. Ionic Channels of Excitable Membranes. Third edition. Sinauer Associates Inc., Sunderland, MA. 814 pp.

Hodgkin, A.L., and A.F. Huxley. 1952. A quantitative description of membrane current and its application to conduction and excitation in nerve. *J. Physiol.* 117:500–544. https://doi.org/10.1113/jphysiol.1952.sp004764

Hollins, B., and S.R. Ikeda. 1996. Inward currents underlying action potentials in rat adrenal chromaffin cells. *J. Neurophysiol.* 76:1195–1211. https://doi.org/10.1152/jn.1996.76.2.1195

Horn, R., and A. Marty. 1988. Muscarinic activation of ionic currents measured by a new whole-cell recording method. *J. Gen. Physiol.* 92:145–159. https://doi.org/10.1085/jgp.92.2.145

Jones, S.W. 1987. Sodium currents in dissociated bull-frog sympathetic neurones. *J. Physiol.* 389:605–627. https://doi.org/10.1113/jphysiol.1987.sp016674

Kaczmarek, L.K., A. Bhattacharjee, R. Desai, L. Gan, P. Song, C.A. von Hehn, M.D. Whim, and B. Yang. 2005. Regulation of the timing of MNTB neurons by short-term and long-term modulation of potassium channels. *Hear. Res.* 206:133–145. https://doi.org/10.1016/j.heares.2004.11.023

Khaliq, Z.M., N.W. Gouwens, and I.M. Raman. 2003. The contribution of resurgent sodium current to high-frequency firing in Purkinje neurons: an experimental and modeling study. *J. Neurosci.* 23:4899–4912. https://doi.org/10.1523/JNEUROSCI.23-12-04899.2003

Kilpatrick, D.L., R.V. Lewis, S. Stein, and S. Udenfriend. 1980. Release of enkephalins and enkephalin-containing polypeptides from perfused beef adrenal glands. *Proc. Natl. Acad. Sci. USA.* 77:7473–7475. https://doi.org/10.1073/pnas.77.12.7473

Kuo, C.C., and B.P. Bean. 1994. Na^+ channels must deactivate to recover from inactivation. *Neuron.* 12:819–829. https://doi.org/10.1016/0896-6273(94)90335-2

Laezza, F., B.R. Gerber, J.Y. Lou, M.A. Kozel, H. Hartman, A.M. Craig, D.M. Ornitz, and J.M. Nerbonne. 2007. The FGF14(F145S) mutation disrupts the interaction of FGF14 with voltage-gated Na+ channels and impairs neuronal excitability. *J. Neurosci.* 27:12033–12044. https://doi.org/10.1523/JNEUROSCI.2282-07.2007

Laezza, F., A. Lampert, M.A. Kozel, B.R. Gerber, A.M. Rush, J.M. Nerbonne, S.G. Waxman, S.D. Dib-Hajj, and D.M. Ornitz. 2009. FGF14 N-terminal splice variants differentially modulate Nav1.2 and Nav1.6-encoded sodium channels. *Mol. Cell. Neurosci.* 42:90–101. https://doi.org/10.1016/j.mcn.2009.05.007

Lingle, C.J., C.R. Solaro, M. Prakriya, and J.P. Ding. 1996. Calcium-activated potassium channels in adrenal chromaffin cells. *Ion Channels.* 4:261–301. https://doi.org/10.1007/978-1-4899-1775-1_7

Lingle, C.J., P.L. Martinez-Espinosa, L. Guarina, and E. Carbone. 2018. Roles of Na^+, Ca^{2+}, and K^+ channels in the generation of repetitive firing and rhythmic bursting in adrenal chromaffin cells. *Pflugers Arch.* 470:39–52. https://doi.org/10.1007/s00424-017-2048-1

Liu, C.J., S.D. Dib-Hajj, M. Renganathan, T.R. Cummins, and S.G. Waxman. 2003. Modulation of the cardiac sodium channel Nav1.5 by fibroblast growth factor homologous factor 1B. *J. Biol. Chem.* 278:1029–1036. https://doi.org/10.1074/jbc.M207074200

Livett, B.G. 1984. Adrenal medullary chromaffin cells in vitro. *Physiol. Rev.* 64:1103–1161. https://doi.org/10.1152/physrev.1984.64.4.1103

Lou, X.L., X. Yu, X.K. Chen, K.L. Duan, L.M. He, A.L. Qu, T. Xu, and Z. Zhou. 2003. Na+ channel inactivation: a comparative study between pancreatic islet beta-cells and adrenal chromaffin cells in rat. *J. Physiol.* 548:191–202. https://doi.org/10.1113/jphysiol.2002.034405

Lou, J.Y., F. Laezza, B.R. Gerber, M. Xiao, K.A. Yamada, H. Hartmann, A.M. Craig, J.M. Nerbonne, and D.M. Ornitz. 2005. Fibroblast growth factor 14 is an intracellular modulator of voltage-gated sodium channels. *J. Physiol.* 569:179–193. https://doi.org/10.1113/jphysiol.2005.097220

Mahapatra, S., A. Marcantoni, A. Zuccotti, V. Carabelli, and E. Carbone. 2012. Equal sensitivity of Cav1.2 and Cav1.3 channels to the opposing modulations of PKA and PKG in mouse chromaffin cells. *J. Physiol.* 590: 5053–5073. https://doi.org/10.1113/jphysiol.2012.236729

Martinez-Espinosa, P.L., C. Yang, V. Gonzalez-Perez, X.M. Xia, and C.J. Lingle. 2014. Knockout of the BK β2 subunit abolishes inactivation of BK currents in mouse adrenal chromaffin cells and results in slow-wave burst activity. *J. Gen. Physiol.* 144:275–295. https://doi.org/10.1085/jgp.201411253

Martinez-Espinosa, P.L., C. Yang, X.M. Xia, and C.J. Lingle. 2021. Nav1.3 and FGF14 are primary determinants of the TTX-sensitive sodium current in mouse adrenal chromaffin cells. *J. Gen. Physiol.* 153. e202012785. https://doi.org/10.1085/jgp.202012785

Milescu, L.S., T. Yamanishi, K. Ptak, and J.C. Smith. 2010. Kinetic properties and functional dynamics of sodium channels during repetitive spiking in a slow pacemaker neuron. *J. Neurosci.* 30:12113–12127. https://doi.org/10.1523/JNEUROSCI.0445-10.2010

Navarro, M.A., A. Salari, J.L. Lin, L.M. Cowan, N.J. Penington, M. Milescu, and L.S. Milescu. 2020. Sodium channels implement a molecular leaky integrator that detects action potentials and regulates neuronal firing. *eLife.* 9:e54940. https://doi.org/10.7554/eLife.54940

Neely, A., and C.J. Lingle. 1992. Two components of calcium-activated potassium current in rat adrenal chromaffin cells. *J. Physiol.* 453:97–131. https://doi.org/10.1113/jphysiol.1992.sp019220

O'Leary, M.E., L.Q. Chen, R.G. Kallen, and R. Horn. 1995. A molecular link between activation and inactivation of sodium channels. *J. Gen. Physiol.* 106:641–658. https://doi.org/10.1085/jgp.106.4.641

Olsen, S.K., M. Garbi, N. Zampieri, A.V. Eliseenkova, D.M. Ornitz, M. Goldfarb, and M. Mohammadi. 2003. Fibroblast growth factor (FGF) homologous factors share structural but not functional homology with FGFs. *J. Biol. Chem.* 278:34226–34236. https://doi.org/10.1074/jbc.M303183200

Patton, D.E., J.W. West, W.A. Catterall, and A.L. Goldin. 1992. Amino acid residues required for fast Na(+)-channel inactivation: charge neutralizations and deletions in the III-IV linker. *Proc. Natl. Acad. Sci. USA.* 89: 10905–10909. https://doi.org/10.1073/pnas.89.22.10905

Rae, J., K. Cooper, P. Gates, and M. Watsky. 1991. Low access resistance perforated patch recordings using amphotericin B. *J. Neurosci. Methods.* 37:15–26. https://doi.org/10.1016/0165-0270(91)90017-T

Role, L.W., and R.L. Perlman. 1980. Purification of adrenal medullary chromaffin cells by density gradient centrifugation. *J. Neurosci. Methods.* 2: 253–265. https://doi.org/10.1016/0165-0270(80)90014-X

Rudy, B. 1978. Slow inactivation of the sodium conductance in squid giant axons. Pronase resistance. *J. Physiol.* 283:1–21. https://doi.org/10.1113/jphysiol.1978.sp012485

Rudy, B. 1981. Inactivation in Myxicola giant axons responsible for slow and accumulative adaptation phenomena. *J. Physiol.* 312:531–549. https://doi.org/10.1113/jphysiol.1981.sp013642

Ruff, R.L. 1996. Sodium channel slow inactivation and the distribution of sodium channels on skeletal muscle fibres enable the performance properties of different skeletal muscle fibre types. *Acta Physiol. Scand.* 156:159–168. https://doi.org/10.1046/j.1365-201X.1996.189000.x

Rush, A.M., E.K. Wittmack, L. Tyrrell, J.A. Black, S.D. Dib-Hajj, and S.G. Waxman. 2006. Differential modulation of sodium channel Na(v)1.6 by two members of the fibroblast growth factor homologous factor 2 subfamily. *Eur. J. Neurosci.* 23:2551–2562. https://doi.org/10.1111/j.1460-9568.2006.04789.x

Schofield, G.G., and S.R. Ikeda. 1988. Sodium and calcium currents of acutely isolated adult rat superior cervical ganglion neurons. *Pflugers Arch.* 411: 481–490. https://doi.org/10.1007/BF00582368

Schwindt, P.C., W.J. Spain, R.C. Foehring, M.C. Chubb, and W.E. Crill. 1988. Slow conductances in neurons from cat sensorimotor cortex in vitro and their role in slow excitability changes. *J. Neurophysiol.* 59:450–467. https://doi.org/10.1152/jn.1988.59.2.450

Shakkottai, V.G., M. Xiao, L. Xu, M. Wong, J.M. Nerbonne, D.M. Ornitz, and K.A. Yamada. 2009. FGF14 regulates the intrinsic excitability of cerebellar Purkinje neurons. *Neurobiol. Dis.* 33:81–88. https://doi.org/10.1016/j.nbd.2008.09.019

Silva, J. 2014. Slow inactivation of Na(+) channels. *Handb. Exp. Pharmacol.* 221: 33–49. https://doi.org/10.1007/978-3-642-41588-3_3

Solaro, C.R., M. Prakriya, J.P. Ding, and C.J. Lingle. 1995. Inactivating and noninactivating $Ca^{(2+)}$- and voltage-dependent K^+ current in rat adrenal chromaffin cells. *J. Neurosci.* 15:6110–6123. https://doi.org/10.1523/JNEUROSCI.15-09-06110.1995

Tamura, R., T. Nemoto, T. Maruta, S. Onizuka, T. Yanagita, A. Wada, M. Murakami, and I. Tsuneyoshi. 2014. Up-regulation of NaV1.7 sodium channels expression by tumor necrosis factor-α in cultured bovine adrenal chromaffin cells and rat dorsal root ganglion neurons. *Anesth. Analg.* 118:318–324. https://doi.org/10.1213/ANE.0000000000000085

Vandael, D.H., A. Zuccotti, J. Striessnig, and E. Carbone. 2012. Ca(V)1.3-driven SK channel activation regulates pacemaking and spike frequency adaptation in mouse chromaffin cells. *J. Neurosci.* 32:16345–16359. https://doi.org/10.1523/JNEUROSCI.3715-12.2012

Vandael, D.H., A. Marcantoni, and E. Carbone. 2015a. Ca1.3 channels as key regulators of neuron-like firings and catecholamine release in chromaffin cells. *Curr. Mol. Pharmacol.* 8:149–161. https://doi.org/10.2174/1874467208666150507105443

Vandael, D.H., M.M. Ottaviani, C. Legros, C. Lefort, N.C. Guérineau, A. Allio, V. Carabelli, and E. Carbone. 2015b. Reduced availability of voltage-gated sodium channels by depolarization or blockade by tetrodotoxin boosts burst firing and catecholamine release in mouse chromaffin cells. *J. Physiol.* 593:905–927. https://doi.org/10.1113/jphysiol.2014.283374

Venkatesan, K., Y. Liu, and M. Goldfarb. 2014. Fast-onset long-term open-state block of sodium channels by A-type FHFs mediates classical spike accommodation in hippocampal pyramidal neurons. *J. Neurosci.* 34: 16126–16139. https://doi.org/10.1523/JNEUROSCI.1271-14.2014

Wada, A., E. Wanke, F. Gullo, and E. Schiavon. 2008. Voltage-dependent Na(v)1.7 sodium channels: multiple roles in adrenal chromaffin cells and peripheral nervous system. *Acta Physiol. (Oxf.).* 192:221–231. https://doi.org/10.1111/j.1748-1716.2007.01810.x

Wang, L.Y., L. Gan, I.D. Forsythe, and L.K. Kaczmarek. 1998. Contribution of the Kv3.1 potassium channel to high-frequency firing in mouse auditory neurones. *J. Physiol.* 509:183–194. https://doi.org/10.1111/j.1469-7793.1998.183bo.x

Wang, C., B.C. Chung, H. Yan, S.Y. Lee, and G.S. Pitt. 2012. Crystal structure of the ternary complex of a NaV C-terminal domain, a fibroblast growth factor homologous factor, and calmodulin. *Structure.* 20:1167–1176. https://doi.org/10.1016/j.str.2012.05.001

West, J.W., D.E. Patton, T. Scheuer, Y. Wang, A.L. Goldin, and W.A. Catterall. 1992. A cluster of hydrophobic amino acid residues required for fast Na(+)-channel inactivation. *Proc. Natl. Acad. Sci. USA.* 89:10910–10914. https://doi.org/10.1073/pnas.89.22.10910

Wittmack, E.K., A.M. Rush, M.J. Craner, M. Goldfarb, S.G. Waxman, and S.D. Dib-Hajj. 2004. Fibroblast growth factor homologous factor 2B: association with Nav1.6 and selective colocalization at nodes of Ranvier of dorsal root axons. *J. Neurosci.* 24:6765–6775. https://doi.org/10.1523/JNEUROSCI.1628-04.2004

Zhang, Z., Z. Zhao, Y. Liu, W. Wang, Y. Wu, and J. Ding. 2013. Kinetic model of Nav1.5 channel provides a subtle insight into slow inactivation associated excitability in cardiac cells. *PLoS One.* 8:e64286. https://doi.org/10.1371/journal.pone.0064286

Supplemental material

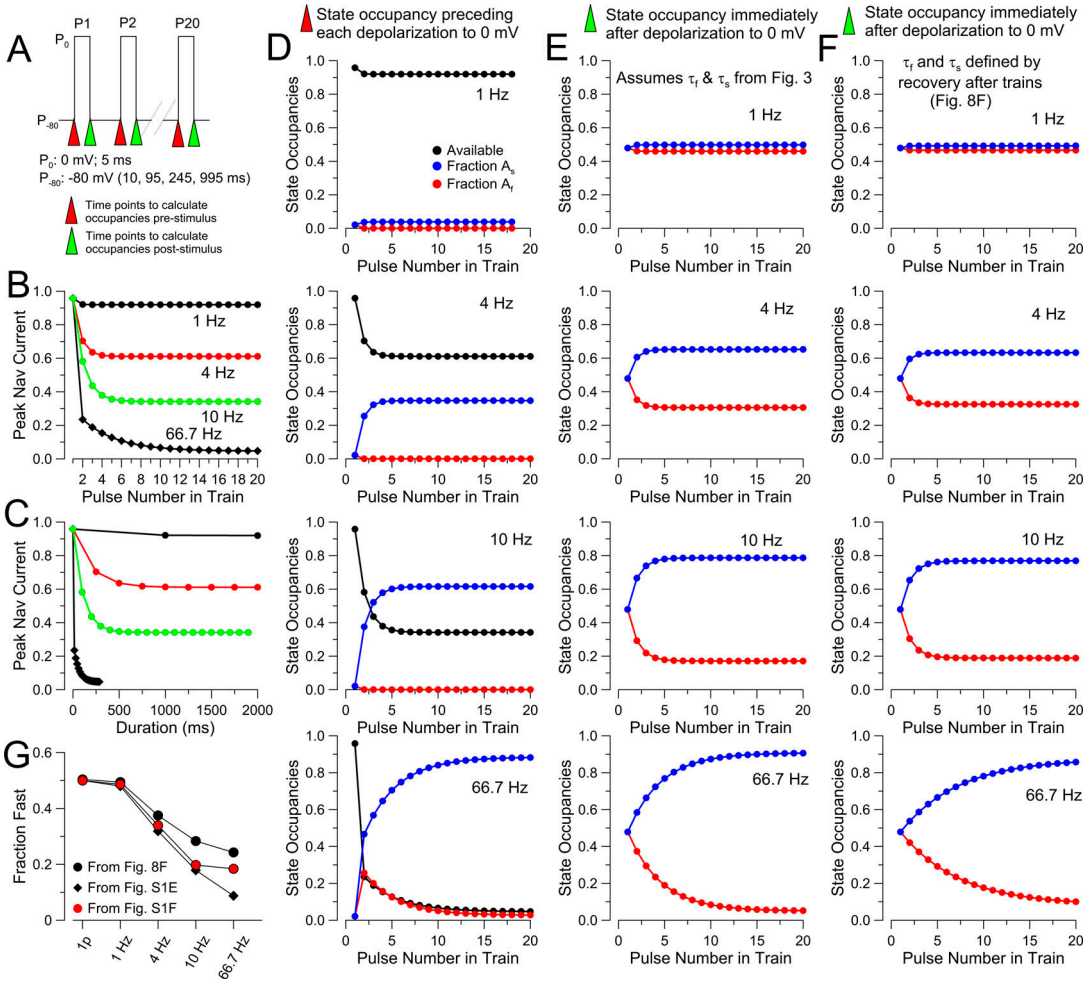

Figure S1. **Predicted state occupancies and peak current decrement during trains of different frequencies. (A)** Schematic of pulse train design and time points used for calculation of occupancies. Trains of twenty 5-ms depolarizations to 0 mV were evoked from a holding potential of −80 mV (e.g., Fig. 8), with interpulse intervals of 10 ms (66.7 Hz), 95 ms (10 Hz), 245 ms (4 Hz), or 995 ms (1 Hz). Red arrows mark time points immediately before depolarizations to 0 mV, at which occupancies prestimulus were determined. The fraction of noninactivated channels at this point defines the effective peak current activated during the subsequent depolarization. Green arrows mark the time point immediately after termination of the depolarizing pulse. The fraction of channels in slow- and fast-recovering inactivated states defines the fraction of fast- and slow-recover components that one would predict during recovery intervals begun at these time points. To determine fractional occupancies, the following assumptions and calculations were made. First, beginning from a holding potential of −80 mV and from the steady-state inactivation curve of Fig. 1 E, the fraction of available channels is 0.95, with 0.025 each in slow and fast inactivated states. Second, we assume that whatever the fraction of channels activated by a depolarization, half will inactivate into fast recovery pathways and half into slow recovery pathways. Third, the fraction of channels that inactivated into each path during the 5-ms depolarization are incremented by the fraction of channels that remained in fast and slow recovery paths before the depolarization. These sums then define the fractions of channels in fast and slow recovery paths, if recovery was then allowed to proceed. Fourth, for each recovery interval (whether 10, 95, 245, or 995 ms), the time constants for fast and slow recovery from Fig. 3 C at −80 mV were used to calculate the fraction of fast or slow inactivated channels that would be expected to recover from inactivation during that interval. This then allows determination of the fractional occupancies before each subsequent depolarization. **(B)** The decrement in peak Nav current based on determination of fractional availability before each 5-ms depolarization was determined and plotted as a function of number of the pulse in a train for each of the indicated frequencies based on inactivation time constants from Fig. 3. Compare with measured decrements in depolarization-evoked Nav currents during trains in Fig. 8. **(C)** Replot of the values in B as a function of time. **(D)** The calculated state occupancies for channels available for activation (immediately before each 5-ms depolarization), channels in fast recovery inactvated states, and channels in slow recovery inactivated states are plotted for, from top to bottom, trains of 1, 4, 10, and 66.7 Hz. Note that for train frequencies or 1, 4, and 10 Hz, essentially all channels that inactivate into fast recovery inactivated states recover from inactivation between each depolarization, while at 66.7 Hz, there is an initial increase in the fraction of channels in fast recovery states for early pulses, which then decreases as occupancy of channels in slow recovery states increases. **(E)** State occupancies for channels in fast recovery pathways and slow recovery pathways immediately following the 5-ms depolarization are plotted for, from top to bottom, trains at 1, 4, 10, and 66.7 Hz, respectively. In all cases, time constants were taken from Fig. 3 C (τ_f = 16 ms; τ_s = 388 ms) and used for all trains. **(F)** As in E, but values for τ_f and τ_s were assumed to vary with train frequency as in Fig. 8 G, for which τ_f becomes slower as train frequency is increased. For train frequencies of 1, 4, and 10 Hz, the recovery intervals are sufficiently long that fractional occupancies are similar for the small differences in time constants used. At 66.7 Hz, changes in the fast recovery time constant result in substantial changes in fractional recovery during the 10-ms recovery interval, thereby slowing the decrease in occupancy of channels in fast recovery states. **(G)** Changes in the fraction of fast recovery following a 10-pulse train at various frequencies are plotted, showing the data plotted from Fig. 8 F, along with the calculated occupancy of fast recovery states from E, and also the occupancies from F. Although peak current amplitudes during a train at 10 Hz fall to levels <0.05, depending on apparent time constants of fast inactivation, fractional occupancy of channels in fast recovery states can still be as much as 0.2, generally consistent with experimental observations (Fig. 7 E and Fig. 8 G).

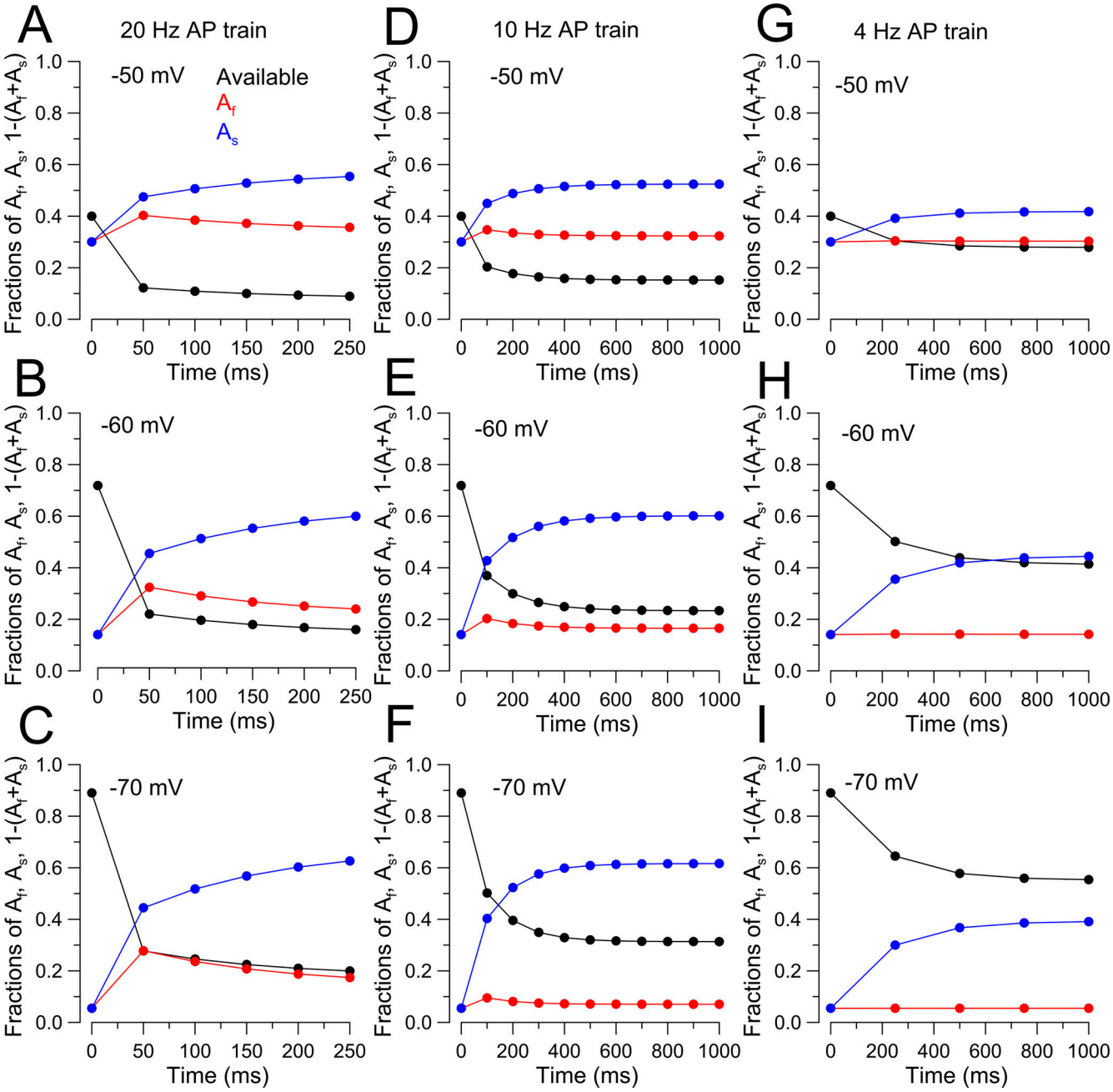

Figure S2. **Calculated fractional occupancies of fast and slow recovery pathways during AP clamp waveform trains.** Strategy for calculation of occupancies follows that in Fig. S1, with identical assumptions with initial state occupancies defined by the steady-state availability curve (Fig. 1 E; 0.958 [−80 mV], 0.890 [−70 mV], −0.719 [−60 mV], 0.400 [−50 mV]), and that initial depolarization leads to even distribution between fast and slow recovery paths. For the impact of the afterhyperpolarization, we assumed a 34.6-ms afterhyperpolarization centered at −50 mV. For 4-Hz stimulation, there is then a 200.2-ms interval at the holding potential; for 10 Hz, there is 49.8 ms; and for 20 Hz, only 1.4 ms. Thus, for 20-Hz stimulation, the recovery is dominated by the tail current period at −50 mV, rather than the holding potential. For the AP clamp waveform, there is also 5 ms at −50 mV that precedes the upswing of the AP voltage waveform. Given the slow rates of onset or recovery from inactivation, this 5-ms interval has negligible impact on changes in occupancy of inactivated states. This procedure essentially defines the expected state occupancies immediately preceding each AP. **(A–C)** Calculated state occupancies for a 20-Hz AP train for −50, −60, and −70 mV holding potentials are shown. Following the initial AP waveform, at the time of the second AP waveform, there is increased occupancy of both fast- and slow-recovering pathways, but with subsequent Aps, the fraction of channels in slow recovery pathways increases, while those in fast recovery pathways decreases. **(D–F)** State occupancies are plotted for the 10-Hz cases, qualitatively exhibiting behavior similar to that for 20 Hz. **(G–I)** State occupancies plotted for the 4 Hz-trains.